Molecular Mechanisms Underlying Medium-Chain Free Fatty Acid-regulated Activity of the Phospholipase PlaF from *Pseudomonas aeruginosa*

Rocco Gentile[1], Matea Modric[2], Björn Thiele[3], Karl-Erich Jaeger[2,4], Filip Kovacic[2,*], Stephan Schott-Verdugo[5], Holger Gohlke[1,5,*]

1. Institute for Pharmaceutical and Medicinal Chemistry, Heinrich Heine University Düsseldorf, 40225 Düsseldorf, Germany
2. Institute of Molecular Enzyme Technology, Heinrich Heine University Düsseldorf, Forschungszentrum Jülich GmbH, 52425 Jülich, Germany
3. Institute of Bio- and Geosciences (IBG-2: Plant Sciences and IBG-3: Agrosphere), Forschungszentrum Jülich GmbH, 52425 Jülich, Germany
4. Institute of Bio- and Geosciences (IBG-1: Biotechnology), Forschungszentrum Jülich GmbH, 52425 Jülich, Germany
5. Institute of Bio- and Geosciences (IBG-4: Bioinformatics), Forschungszentrum Jülich GmbH, 52425 Jülich, Germany

Running title: Product Feedback Regulation of Phospholipase A PlaF

Keywords: molecular dynamics simulations, membrane, dimerization, tilting, potential of mean force, decanoic acid, inhibition

*Corresponding authors:

Prof. Dr. Holger Gohlke
Institute for Pharmaceutical and Medicinal Chemistry, Heinrich Heine University Düsseldorf, Universitätstr. 1, 40225 Düsseldorf, Germany
and
Institute of Bio- and Geosciences (IBG-4: Bioinformatics), Forschungszentrum Jülich GmbH, Wilhelm-Johnen-Str., 52425 Jülich, Germany
Email: gohlke@uni-duesseldorf.de or h.gohlke@fz-juelich.de

Dr. Filip Kovacic
Institute of Molecular Enzyme Technology (IMET), Heinrich Heine University Düsseldorf and Forschungzentrum Jülich GmbH, Wilhelm-Johnen-Str., 52425 Jülich, Germany
Email: f.kovacic@fz-juelich.de

ABSTRACT

PlaF is a membrane-bound phospholipase A_1 from *P. aeruginosa* that is involved in remodeling membrane glycerophospholipids (GPLs) and modulation of virulence-associated signaling and metabolic pathways. Previously, we identified the role of medium-chain free fatty acids (FFA) in inhibiting PlaF activity and promoting homodimerization, yet the underlying molecular mechanism remained elusive. Here, we used unbiased and biased molecular dynamics simulations and free energy computations to assess how PlaF interacts with FFAs localized in the water milieu surrounding the bilayer or within the bilayer, and how these interactions regulate PlaF activity. Medium-chain FFAs localized in the upper bilayer leaflet can stabilize inactive dimeric PlaF, likely through interactions with charged surface residues as experimentally validated. Potential of mean force (PMF) computations indicate that membrane-bound FFAs may facilitate the activation of monomeric PlaF by lowering the activation barrier of changing into a tilted, active configuration. We estimated that the coupled equilibria of PlaF monomerization-dimerization and tilting at the physiological concentration of PlaF lead to the majority of PlaF forming inactive dimers when in a cell membrane loaded with decanoic acid (C10). This is in agreement with a suggested *in vivo* product feedback loop and GC-MS profiling results indicating that PlaF catalyzes the release of C10 from *P. aeruginosa* membranes. Additionally, we found that C10 in the water milieu can access the catalytic site of active monomeric PlaF, contributing to the competitive component of C10-mediated PlaF inhibition. Our study provides mechanistic insights into how medium-chain FFA may regulate the activity of PlaF, a potential bacterial drug target.

54 **1. INTRODUCTION**

55 The Gram-negative bacterium *P. aeruginosa* is a human pathogen and a frequent cause of nosocomial
56 infections, affecting primarily immune-compromised patients (1, 2). A large spectrum of virulence
57 factors contributes to the pathogenicity of *P. aeruginosa* (3). Among these, type A phospholipases
58 (PLA_1) participate in host membrane damage and modulation of various signaling networks in infected
59 cells (4, 5). PLA_1 hydrolyzes membrane GPL at the *sn*-1 position yielding lysoglycerophospholipid
60 (LGPL) and FFA (6, 7). GPLs are membrane components involved in cellular integrity and regulation
61 of membrane protein function and stability (8). The alteration of the membrane GPL composition has
62 been linked to biofilm formation, growth phase transition, virulence, and cytotoxicity of *P. aeruginosa*
63 (1, 2, 6, 9). On the other side, FFA in *P. aeruginosa* acts as a signaling molecule (10) or as the precursor
64 of signal molecules including the hydroxy-alkylquinolines (11), diffusible signal factors or oxylipin
65 autoinducer (12) families, important for bacterial virulence in the pathogen (13).
66 Previously, we showed that *P. aeruginosa* PlaF is a cytoplasmic membrane-bound PLA_1 that contributes
67 to the alteration of the membrane GPL profile and virulence properties of this bacterium (6). *In vitro*
68 enzyme activity experiments showed a specificity of PlaF towards GPLs and LGPLs with medium-chain
69 acyl moieties (10 - 14 carbon atoms), while short- and long-chain GPLs are only poorly hydrolyzed (6,
70 15). A high-resolution crystal structure of PlaF, combined with homodimerization studies by
71 crosslinking, micro-scale thermophoresis, and molecular simulations, has revealed that PlaF can adopt
72 both monomeric and dimeric configurations **(Figure 1)** (6). However, only the monomeric state of the
73 protein was found to be catalytically active. The crystal structure revealed a homodimer characterized
74 by interactions between the transmembrane (TM) and juxtamembrane (JM) regions between the single
75 monomers. The crystal structure of the PlaF dimer revealed the co-crystallized endogenous ligands
76 undecanoic acid (11A) and tetradecanoic acid (myristic acid, MYR) in the catalytic site of each
77 monomer, with their acyl chains occupying tunnel 1 (T1) pointing towards the dimeric interface (6).
78 Free energy computations (16) and experiments indicated that, at physiological protein concentrations,
79 the equilibrium between the PlaF dimer and the monomers is shifted to the latter side in the cell (6). In
80 the dimeric form, the entrance of T1 resides more than 5 Å above the membrane's upper leaflet, thus

81 hampering GPL substrate access from the membrane in T1 (6). Interestingly, unbiased molecular
82 dynamics (MD) simulations (17) showed that the PlaF monomer undergoes a tilting motion in the
83 membrane, bringing the opening of the catalytic tunnel in close vicinity to the membrane, with free
84 energy computations revealing that the tilted state of the monomeric PlaF (t-PlaF) is energetically more
85 favorable than the non-tilted state, named split or s-PlaF state (**Figure 1**) (6). Consequently, it has been
86 suggested that this tilting motion underlies the activation of the monomeric s-PlaF by facilitating
87 substrate access to the active site tunnel (6).
88 In addition, two other tunnels (T2 and T3) that connect the active site to the surface of PlaF have been
89 identified (15). Unbiased MD simulations suggested that MYR, the hydrolysis product of GPL and
90 LGPL, relocates from T3 and reaches the entrance of T1, in agreement with the positions of
91 cocrystallized ligands MYR and 11A (6, 15). Accordingly, the FFA can reach the membrane bilayer *via*
92 T1. We have recently shown that medium-chain FFAs, containing 10 - 14 carbon atoms, inhibit PlaF
93 activity according to a mixed inhibition mode and that they lead to an increase in the PlaF dimer
94 concentration (6). From our results, we hypothesize that the FFAs may inhibit PlaF activity by two
95 mechanisms: i) allosterically, by impacting the dimer-monomer equilibrium and/or the tilting transition
96 when they are located in the lipid bilayer, and ii) competitively, by interfering with the substrate binding
97 when they enter the active site *via* T3 from the water milieu mimicking the periplasmic space **(Figure**
98 **1)**. However, the detailed molecular mechanisms that govern the PlaF inhibition by FFAs have remained
99 elusive.
100 Here, we combine unbiased and biased all-atom MD simulations (18) and configurational free energy
101 computations (16) to evaluate the effect of FFAs on the structural dynamics and energetics of the PlaF
102 dimer-monomer transition and the monomer tilting and to reveal hot spot PlaF residues potentially
103 involved in the interaction with FFAs. Additionally, we pursue free ligand diffusion MD simulations
104 (19) and binding free energy computations (16) of FFAs located in the water phase near the catalytic
105 domain of PlaF. The suggested FFA binding sites in PlaF and their putative roles in inhibition and
106 dimerization were experimentally studied using site-directed mutagenesis and purified PlaF variants
107 reconstituted into small unilamellar vesicles (SUVs) in inhibition and crosslinking assays.

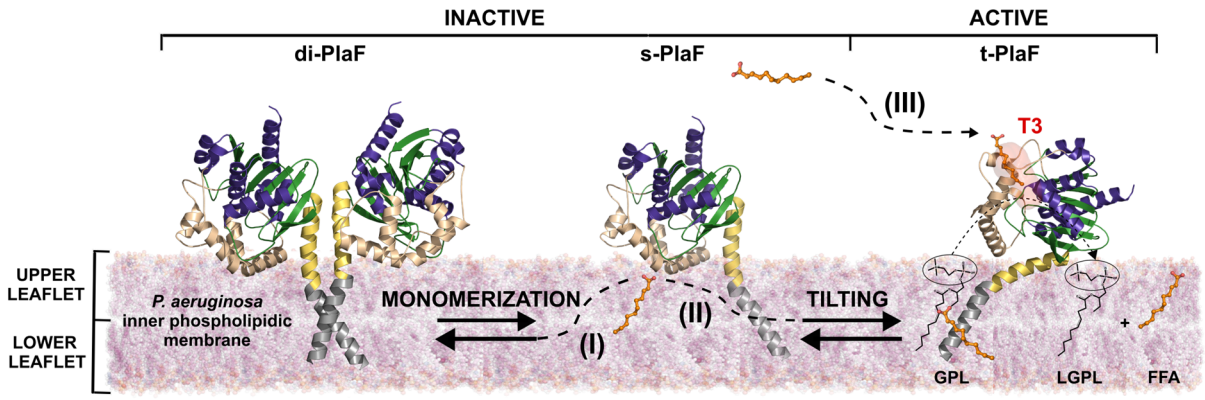

Figure 1. A working model illustrating the possible impact of FFA on the dimer-monomer equilibrium of PlaF and its monomer tilting. PlaF is anchored to the bilayer through a transmembrane (TM) region (grey) predominantly containing hydrophobic residues and a juxtamembrane (JM) region (yellow) rich in polar and charged residues. The JM domain is in close contact with the polar heads of the phospholipid membrane when PlaF is tilted. The C-terminal catalytic domain points towards the periplasm and is characterized by an α/β hydrolase fold (green, violet) providing the scaffold for the catalytic triad (Ser, Asp, His) and Arg-Lys-rich lid-like (LL, light brown) domain that presumably interacts with the phospholipid bilayer. PlaF can adopt a dimeric (di-PlaF) or monomeric configuration (s-PlaF), and the monomer can tilt (t-PlaF). The t-PlaF monomer is considered the active form (6). Lipid bilayer-bound FFA (orange), generated by PlaF from GPL or LGPL, may influence the dimer-monomer equilibrium (I) and/or the tilting transition (II) and/or enter PlaF from the water milieu (III) through tunnel 3 (T3).

122 **2. RESULTS**

123 **2.1 Medium-chain Fatty Acids are Detected in *P. aeruginosa* in Free Form and Likely Originate**
124 **from Glycerophospholipid Hydrolysis**

125 Our previous lipidomics analysis by Q-TOF MS/MS revealed that the alteration of the membrane GPL
126 profile of *P. aeruginosa* is linked to PlaF-mediated degradation of several GPLs, including three GPLs
127 containing medium-chain FAs: phosphatidylglycerol (PG) 24:3, phosphatidylethanolamine (PE) 22:1,
128 and phosphatidylinositol (PI) 26:0 (6). In this study, and to evaluate how PlaF modifies the FFA profile
129 and the FFA availability to potentially regulate PlaF activity in the periplasmic space, we analyzed if
130 medium-chain FFAs can be identified in *P. aeruginosa* wild-type (WT) and an isogenic *plaF* mutant
131 (Δ*plaF*) with reduced GPL degrading activity (6). To achieve this, we extracted FFAs from cells and
132 supernatant of both strains using organic solvent and quantified the saturated FFAs with acyl chains of
133 6 to 16 carbon atoms by GC-MS. The FFA profile revealed that both *P. aeruginosa* strains produced
134 various intracellularly and extracellularly located saturated FFAs **(Figure 2)**. As anticipated, the long-
135 chain FFAs were the most abundant, while medium-chain FFAs (C8, C9, C10, C12, and C14) accounted
136 for roughly 10 to 15 % of the total FFA amount. No significant differences in the abundance of cell-
137 associated FFAs between the WT and Δ*plaF* were observed, suggesting that FFAs released by PlaF are
138 either metabolized or secreted into the supernatant. We identified that medium-chain FFAs, namely
139 octanoic (C8), decanoic (C10), dodecanoic (C12), and myristic (C14) acids, were significantly less
140 abundant ($p < 0.05$) in the supernatant of Δ*plaF* than the WT.

141 To further explore the possibility that PlaF releases the identified medium-chain FAs from GPLs, we
142 conducted a re-analysis of our published lipidomics results obtained with the Δ*plaF* mutant (6). Our
143 previous analysis had assessed GPLs at the species level, meaning that only information about the total
144 number of carbon atoms in the acyl chains but not their specific identities had been obtained. Thus, we
145 focused on GPL species with up to 24 carbon atoms in their acyl chains, as they likely contain at least
146 one medium-length acyl chain (**Table S1**). Our results show that the *P. aeruginosa* membrane contains
147 56 different medium-chain length GPLs out of a total of 324 identified GPL species (**Table S1**). A
148 comparison of the amount of medium-chain length GPLs relative to the total GPL amount in WT and

149 Δ*plaF* revealed that more (20.8 %) medium-chain length GPLs were identified in the Δ*plaF* mutant than
150 the WT (12.6 %) (**Table S2**). These results together with the specificity of PlaF to hydrolyze medium-
151 chain GPLs (6) suggest that the identified medium-chain FFAs could potentially be generated by PlaF-
152 catalyzed hydrolysis of GPLs.

153 The GC-MS analysis revealed an interesting finding: the extracellular octanoic acid amount was nearly
154 double ($p < 0.001$) that of the intracellular amount in both the WT and Δ*plaF* strains, suggesting that
155 this FFA is predominantly secreted into the supernatant. In contrast, dodecanoic acid, the second FFA
156 identified as a potential PlaF product, was significantly ($p < 0.001$) more abundant inside the cells of
157 Δ*plaF* than the WT. These results show that the FFA transport is dependent on their chain length, as it
158 was observed previously for *Escherichia coli* and *Saccharomyces cerevisiae* (20). This suggests that
159 some FFAs may have a function as extracellularly secreted compounds, such as signaling messengers
160 (10), while others may be primarily used intracellularly, such as for energy production (21).

161 To conclude, the quantification of intracellular and extracellular FFAs is in agreement with our
162 previously determined ability of PlaF to release FFA *in vitro* from various GPLs (6), and further
163 strengthens the suggested *in vivo* function of PlaF in degrading GPLs containing medium-length acyl
164 chains.

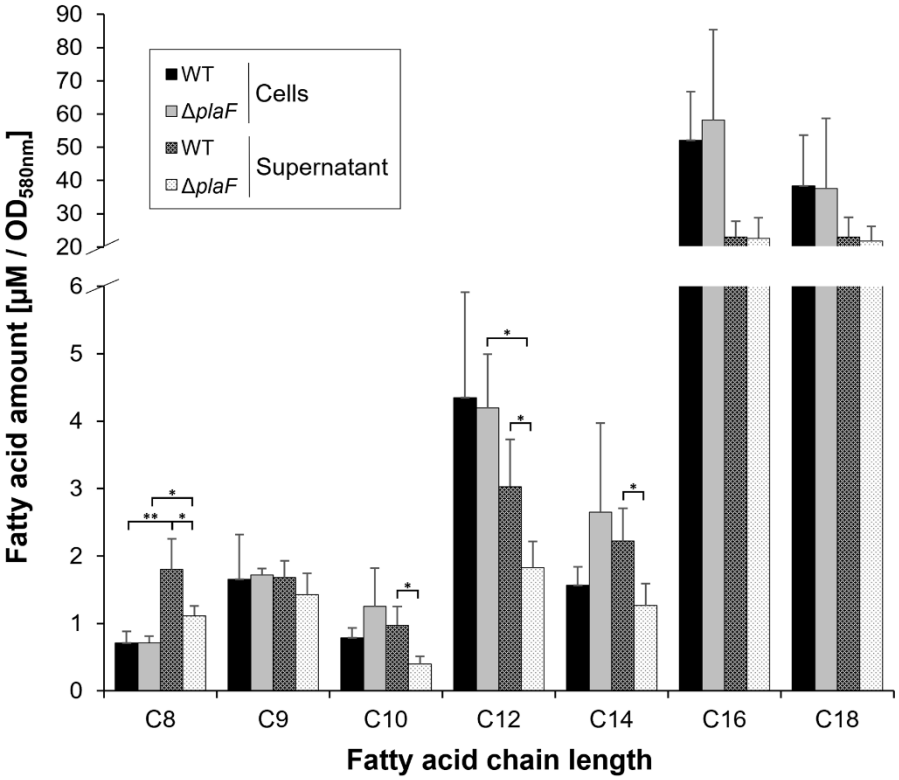

Figure 2: Free fatty acid profile of *P. aeruginosa* WT and Δ*plaF*. Strains were cultivated in LB medium under aeration until the stationary phase, and FFAs were extracted with organic solvent from cells and supernatant. Quantification of FFAs was performed by GC-MS analysis. Means ± SDs are shown ($n = 4$ biological replicates). Statistical analysis was performed using the *t*-test, * $p < 0.05$, ** $p < 0.01$; differences between all other data points were not significant.

2.2 Free Fatty Acids in the Membrane may Facilitate the Tilting of PlaF Monomers

To assess the influence of bilayer-bound FFA on PlaF tilting, we performed all-atom unbiased MD simulations (18) of monomeric PlaF inserted into the lipid bilayer loaded with FFA. The orientations of PlaF obtained after splitting the membrane-embedded PlaF dimer (s-PlaF) or the tilted configuration (t-PlaF) obtained with OPM were considered (22, 23). For each PlaF configuration, two membrane systems were examined, in which C10 or C14 were inserted in the upper leaflet resulting in a DOPE:DOPG:FFA composition of 3:1:1. This system mimics the FFAs bound to the periplasmic leaflet of the inner bacterial membrane, which is interacting with the TM, JM and KR-rich LL domains of PlaF (6). For each system, 12 replicas were simulated, each 1 µs in length, and the results were compared with those obtained previously with PlaF in an FFA-free bilayer composed of DOPE and DOPG at a ratio of 3:1, respectively (6).

When starting from the s-PlaF orientation, a comparable number of transitions to the t-PlaF orientation ("tilting") was observed for the system containing C10 (9/12, 75%) or C14 (10/12, 83%) **(Figure 3)**. These tilting preferences are higher compared to the 50% obtained previously for the system without FFAs (6). These results indicate that FFAs may facilitate the tilting and that for the tested FFA chain length has no influence on the tilting preference. When starting MD simulations from the t-PlaF embedded into the C10- or C14-loaded bilayer, no transition to the s-PlaF orientation was observed **(Figure 3)**, even if the MD simulations were prolonged to 2 µs **(Figure S1)**. These results are in agreement with our previous finding that the tilted orientation of PlaF is preferred (6).

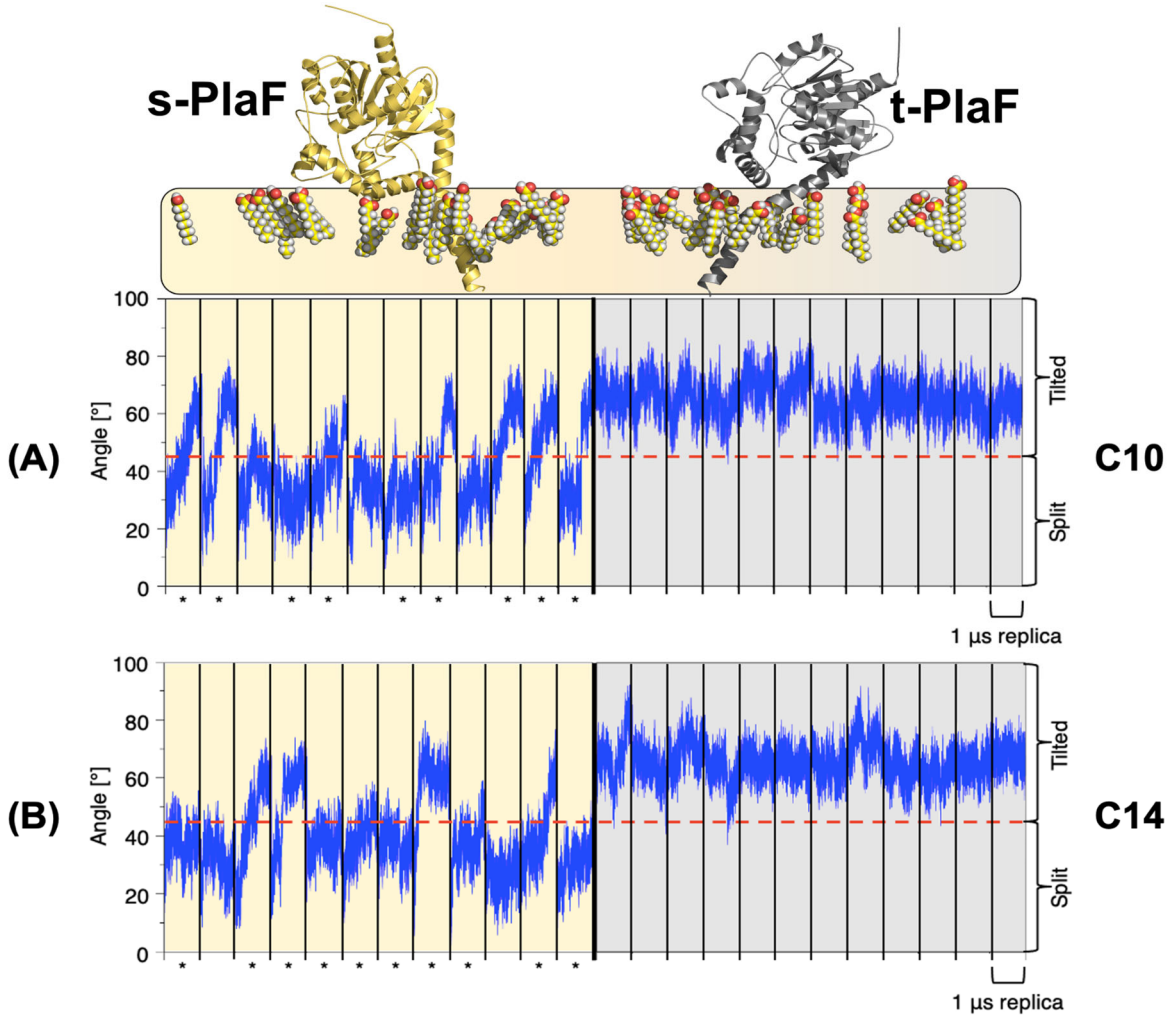

Figure 3. Unbiased MD simulations of monomeric PlaF in the presence of FFA in the upper leaflet. (A) Left (yellow background): Time course of the orientation of PlaF with respect to the bilayer starting from s-PlaF in the presence of C10 at a ratio DOPE:DOPG:C10 of 3:1:1. In 9 of 12 replicas, the s-PlaF adopts a tilted configuration marked with *. Right (grey background): When starting from t-PlaF, the structure remains tilted in all simulations. As before (6), this shows a significant tendency of the monomer to tilt (McNemar's χ^2 = 6.125, p = 0.013). Tilting is

197 quantified by the angle between the membrane normal and the vector between the center of
198 masses (COM) of C_α atoms of residues 21–25 and residues 35–38 and is assumed to occur if
199 the angle is > 45°. **(B)** As in panel A, but now with C14 at a ratio of DOPE:DOPG:C14 of 3:1:1.
200 In 10 of 12 replicas, s-PlaF adopted a tilted configuration (marked with *, McNemar's χ^2 =
201 8.100, p = 0.004) while t-PlaF did not undergo a transition to s-PlaF.
202

203 **2.3 Free Fatty Acids Favor Monomer Tilting but Disfavor Dimer Dissociation**

204 To determine the effect of FFAs in the upper leaflet on the energetics of the PlaF dimer-to-monomer
205 and s-PlaF-to-t-PlaF transitions, we performed umbrella sampling (US) simulations (24) to compute a
206 PMF (25). As the chain length showed a negligible influence on the tilting behavior in the unbiased MD
207 simulations, we only used a membrane system with DOPE:DOPG:C10 of 3:1:1. The US simulations
208 were performed as in ref. (6), starting from the s-PlaF orientation. The distance between the top of the
209 JM domain, computed as the center of mass (COM) of C_α atoms of residues 33-37, and the membrane
210 center along the membrane normal was used as a reaction coordinate to track the tilting transition. For
211 the dimer-to-monomer transition, we started from the dimer configuration as found in the crystal
212 structure and used the distance between the COMs of C_α atoms of residues 25-38 of each PlaF molecule
213 as a reaction coordinate. For the tilting transition, 43 windows were sampled with 800 ns of sampling
214 time each, of which the first 640 ns were discarded as equilibration. Likewise, for the dimer-to-monomer
215 transition, 75 windows were sampled with 800 ns of sampling time each, of which the first 640 ns were
216 discarded as equilibration. In both cases, the kernel densities showed a median overlap of 34.9 ± 1.4%
217 and 32.2 ± 1.5% between contiguous windows, respectively **(Figures S7 and S8)**, well suited for PMF
218 calculations (26). The standard error of the mean was calculated from free energy profiles determined
219 independently every 20 ns from the last 160 ns per window. The PMF of the titling transition is
220 converged and precise **(Figure S7)**. In the presence of C10 in the bilayer, t-PlaF is preferred over s-PlaF
221 **(Figure 4A)**, which is similar to results without FFA in the bilayer (6). However, the global minimum
222 of t-PlaF is lower by ~4 kcal mol^{-1} in the bilayer containing C10 than the one without C10, indicating
223 that t-PlaF is even more favorable in the presence of C10. Additionally, a local minimum was observed
224 in the system containing C10 instead of a barrier separating the split and tilted PlaF configurations in
225 the system without FFA **(Figure 4A)**. These results are in accordance with the unbiased MD simulations,

226 which indicated that the tilted configuration is preferred and that the transition to it is facilitated in the
227 presence of FFAs.

228 The PMF for the dimer-to-monomer transition was computed considering two bilayer compositions with
229 20 mol% and 33.3 mol% of C10 in the upper leaflet. The PMFs are converged and precise **(Figures S8**
230 **and S9)**. As in the membrane without FFA (6), dimeric PlaF is favored over the monomeric state in the
231 presence of C10 in the membrane **(Figure 4B)**. However, FFA stabilizes the di-PlaF in a concentration-
232 dependent manner by ~10 and ~14 kcal mol^{-1} compared to a system without FFA.

233 To conclude, the PMF computations demonstrated that the presence of C10 within the upper bilayer
234 leaflet promotes the tilting of s-PlaF, corroborating the findings of our MD simulations (**Figure 3A**),
235 and C10 exhibits a concentration-dependent stabilizing effect on the PlaF dimer **(Figure 4C)**.

236

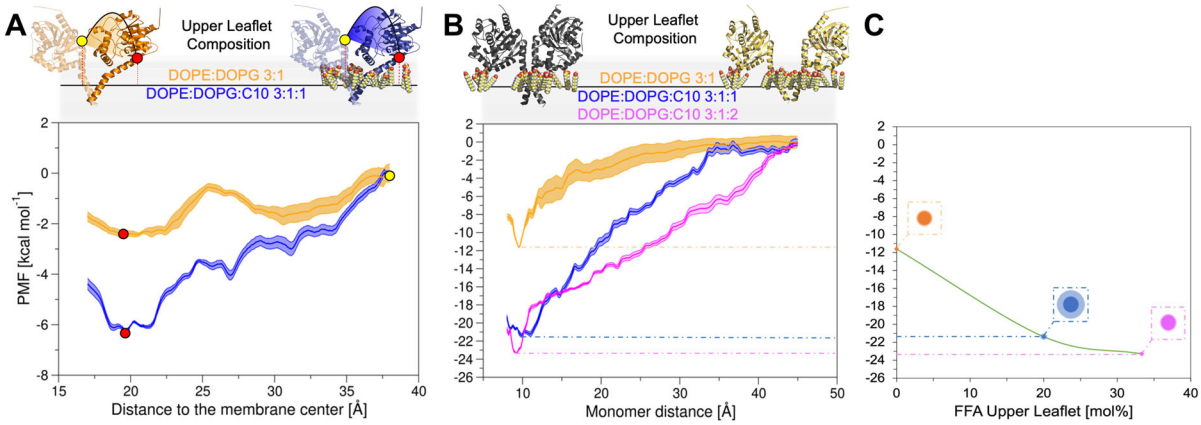

237

238 **Figure 4. PMFs of monomer tilting and dimer separation. (A)** PMF of monomer tilting. The
239 distance along the membrane normal between the COM of C_α atoms of residues 33-37 and the
240 COM of the C18 of the oleic acid moieties of all GPLs in the bilayer was used as a reaction
241 coordinate. Orange: PMF computed for the bilayer consisting of DOPE:DOPG 3:1 (values were
242 taken from ref. (6)). Blue: PMF computed here for the bilayer containing C10 in the upper
243 leaflet at the ratio DOPE:DOPG:C10 of 3:1:1. The shaded areas at the curves show the standard
244 error of the mean (SEM). The yellow and red dots indicate s-PlaF and t-PlaF, respectively. **(B)**
245 PMF of di-PlaF separation. The distance between the COM of C_α atoms of residues 25-38 of
246 each PlaF molecule was used as the reaction coordinate. Orange: PMF values for the bilayer
247 consisting of DOPE:DOPG 3:1 were taken from ref. (6)). Blue: PMF for the bilayer containing
248 C10 in the upper leaflet at the ratio DOPE:DOPG:C10 of 3:1:1. Magenta: PMF computed for
249 the bilayer containing C10 in the upper leaflet at the ratio DOPE:DOPG:C10 of 3:1:2. The
250 shaded areas show the SEM. The black protein on the top shows the PlaF dimer at a monomer
251 distance of ~9.9 Å, and the yellow ones show the completely dissociated PlaF at ~45 Å. **(C)**

252 PMF values at the respective global minima. This panel shows PMF values at the respective
253 global minima from panel B as a function of the C10 concentration in the upper bilayer leaflet.
254 Dashed lines connect respective points in panels B and C. The green line connecting the points
255 illustrates a non-linear correlation between FFA concentration in the upper leaflet and PlaF
256 dimer stabilization. The shaded area around each dot indicates the SEM at the corresponding
257 minimum.
258

259 **2.4 Estimating the Ratio of Monomeric and Dimeric PlaF in the Cell in the Presence of Free Fatty**
260 **Acids**

261 Following previous work by us (6, 27) and others (28), we computed from the PMFs of dimer-to-
262 monomer and tilting transitions with an upper leaflet composition of DOPE:DOPG:C10 of 3:1:1
263 equilibrium constants (K_a = 1.68 × 10^{14} Å^2 (eq. S1), K_x = 2.59 × 10^{12} (eq. S2), $K_{tilting}$ = 1.73 × 10^2 (eq.
264 S5)) and free energies (ΔG = - 17.04 ± 0.22 kcal mol^{-1} (eq. S3), $\Delta G_{tilting}$ = - 3.04 ± 0.20 kcal mol^{-1} (eq.
265 S6)) taking into account that K_x and ΔG relate to a state of one PlaF dimer in a membrane of 1258 GPLs,
266 according to our simulations setup. Experimentally, a concentration of one PlaF dimer per ~3786 GPLs
267 in *P. aeruginosa* PlaF-overexpressing cells was determined (29). However, the concentration in *P.*
268 *aeruginosa* wild-type (WT) is estimated as 100- to 1000-fold lower.

269 Under such physiological conditions in the *P. aeruginosa* WT and considering that the equilibria for
270 dimer-to-monomer transition and tilting are coupled, between 2.3 and 7.3% of the PlaF molecules are
271 predicted to be in a monomeric, tilted, catalytically active state in *P. aeruginosa* when 20 mol% C10 are
272 present in the upper leaflet. In the absence of FFAs, between 74% and 96% of the PlaF molecules were
273 predicted to be in a monomeric, tilted, catalytically active state in *P. aeruginosa* WT (6). *Vice versa*, in
274 the presence of FFA, 92.7 to 97.7% of PlaF are in the dimeric configuration, whereas this is only 4 to
275 26% in the absence of FFA (6). The computed increase in the PlaF dimer concentration agrees with our
276 previous biochemical results showing an increased di-PlaF concentration after incubating purified PlaF
277 with C10 (6). Based on these findings, as well as the GC-MS results **(Figure 2)** that indicate the release
278 of C10 by PlaF *in vivo*, it is plausible to propose that the degradation of GPLs catalyzed by PlaF is
279 inhibited by the produced C10. This inhibition may serve as a protective product-feedback mechanism
280 to prevent cell membrane damage.

281 **2.5 Hot spots of di-PlaF – FFA Interactions in the Upper Leaflet Reduce Experimental Dimer**
282 **Stability when Mutated**

283 To characterize interactions between C10 in the upper leaflet and di-PlaF that may favor dimer
284 formation, we analyzed the trajectories of unbiased MD simulations across 12 replicas. 3D density grids
285 representing the probability density of C10 within the membrane led to the identification of states in
286 which C10 is located at a distance of ≤ 5 Å from the PlaF. To discard short-living di-PlaF-C10 states we
287 analyzed if the RMSD of C10 in two consecutive states is < 1.5 Å, indicating that these states
288 encompassed C10 tightly bound to di-PlaF (see Supplementary results). They were clustered with
289 respect to the minimum distance ε between the clusters starting from ε = 2.0 Å, using the all-atom
290 RMSD as the similarity measure. Gradual increase of ε in 0.5 Å intervals led to a constant population
291 of the largest cluster at ε = 5.0 Å.
292 The five most populated clusters cover 80.5 ± 1.5% (mean ± SEM) of all systems with C10 close to
293 PlaF and 65.8 ± 1.3% of all systems in a trajectory **(Figure 5A)**. Over these clusters, R187 and R217,
294 with positively charged side chains, E216 containing a negatively charged side chain, and A220 with a
295 non-polar side chain were identified as the residues mostly interacting with FFA **(Figure 5B)**. These
296 residues are surface-exposed and located in the LL domain, which according to the model of di-PlaF in
297 the membrane interacts with the bilayer (6).
298 To experimentally test the role of these residues on PlaF dimerization in the GPL bilayer, we mutated
299 by site-directed mutagenesis each of the three charged residues to alanine to obtain the single variants
300 $PlaF_{R187A}$, $PlaF_{E216A}$, and $PlaF_{R217A}$. Furthermore, a variant with two neutralized charges, $PlaF_{R187A\text{-}E216A}$,
301 and variants with one neutralized charge and C10-interacting A220 mutated to glycine, $PlaF_{R187A\text{-}A220G}$
302 and $PlaF_{E216A\text{-}A220G}$, were generated. These six PlaF variants and the wild-type PlaF ($PlaF_{WT}$) were
303 produced in *E. coli* and purified by immobilized metal affinity chromatography (IMAC) in the presence
304 of octyl β-D-glucopyranoside (OG). $PlaF_{WT}$ and variants purified to homogeneity as determined by
305 SDS-PAGE **(Figure S10A)** showed comparable thermal stability as determined by nano differential
306 scanning fluorimetry (nanoDSF) **(Table S4)**. These results indicate that the mutations did not markedly

307 destabilize the protein, as mutations of surface-exposed residues are on average considerably less
308 destabilizing compared to mutations of core residue positions (30).
309 Furthermore, we removed OG **(Figure S10B)** and reconstituted $PlaF_{WT}$ and variants into SUVs made of
310 DOPE and DOPG, and C10 was added to reach 20% mol. In the experimental setup, the pH was 8,
311 surpassing the p*K*a value of C10 (6.4), such that C10 is predominantly in a deprotonated and non-
312 micellized state (31). In this state, C10 has limited permeability through the phospholipid bilayer,
313 consequently favoring its partitioning within the outer leaflet (32). This experimental system closely
314 approximates the computational model, rendering it suitable for subsequent comparison with
315 computational data.
316 A quantitative crosslinking assay **(Figure S11)** using the bifunctional reagent dimethyl pimelimidate
317 (DMP), which covalently stabilizes dimers, revealed that C10 triggers the formation of $PlaF_{WT}$ dimers
318 **(Figure 5C)**, as shown before (6). We observed 70% more $PlaF_{WT}$ dimer in the C10-treated sample
319 compared to the untreated one. In contrast, all PlaF variants showed a significantly reduced ability to
320 dimerize in the presence of C10. For single variants, relative amounts of di-PlaF in C10-treated samples
321 were approximatively equal compared to untreated samples. In double-point variants, less di-PlaF in
322 C10-treated than C10-untreated samples was observed. These results indicate that residues predicted by
323 MD simulations to interact with C10 within the bilayer play an important role in C10-triggered PlaF
324 dimerization.

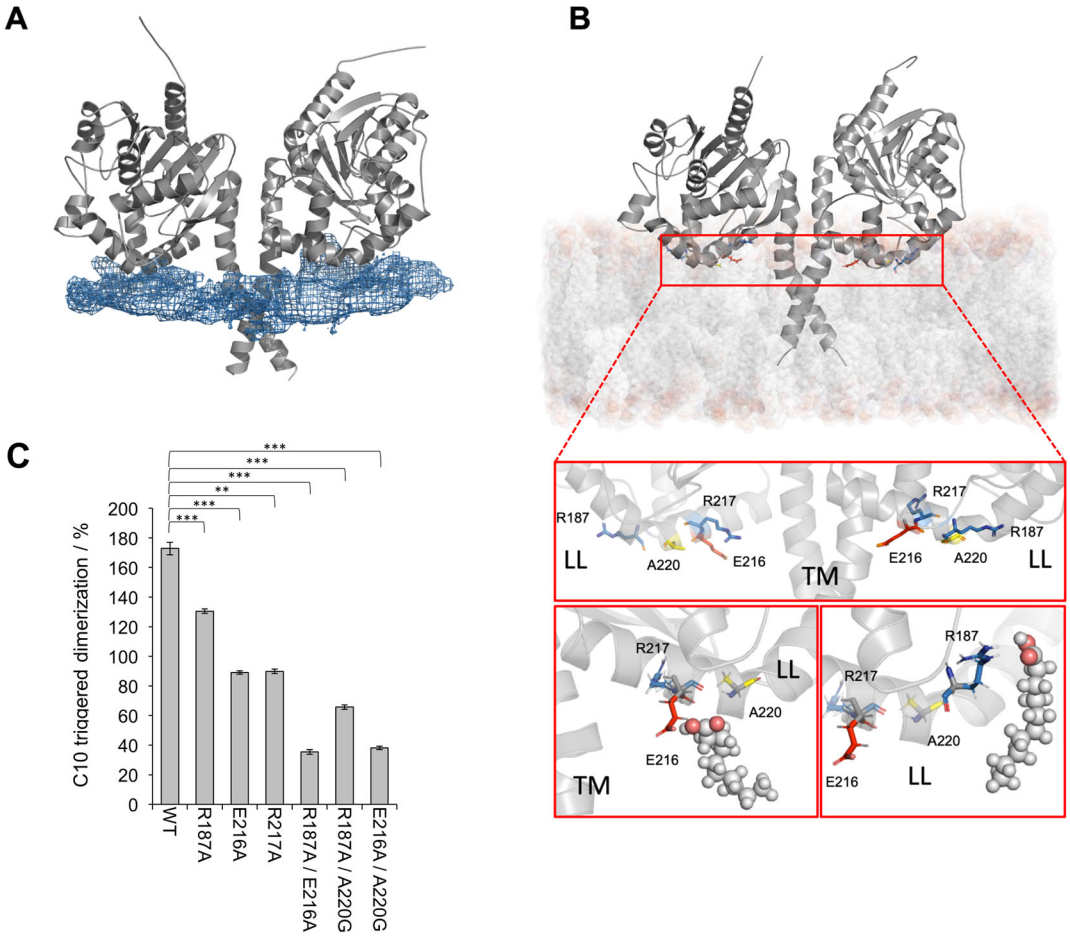

Figure 5. Interaction of C10 located within the upper leaflet with di-PlaF. (A) Average density map of all C10 molecules. 3D density grid illustrating the distribution of all C10 computed with CPPTRAJ (33). The C10 distribute around both monomers in similar proportions. **(B)** Hot spots of di-PlaF-C10 interactions. Hot spots were defined as residues with a distance to C10 ≤ 5 Å and where C10 has an RMSD < 1.5 Å with respect to the previous pose. The red box contains the negatively and positively charged hot spots, shown in red and blue sticks, respectively, while non-polar ones are reported in yellow sticks; LL, the lid-like domain; TM, the transmembrane domain. Red frames at the bottom show enlarged interaction regions with C10 shown in space-fill format (grey, carbon; red, oxygen). The left panel indicates the interaction of C10 with E216 and R217. The right panel indicates the interaction of C10 with R187. **(C)** Effect of mutations in the LL domain on PlaF dimerization. PlaFWT or PlaF variants reconstituted into DOPE:DOPG SUVs were treated with C10 (12 mM) and crosslinker DMP for 2 h at room temperature. SUV reconstituted proteins treated with DMP and DMSO (used as C10 solvent) served as the control without C10. Proteins were separated by SDS-PAGE, followed by Western blot detection of PlaF using anti-His-tag antibodies. The intensities of di-PlaF bands were quantified by ImageJ (34). The results represent the ratio between C10-untreated and C10-treated samples shown as mean ± SD (n = 4).

2.6 Free Fatty Acids in the Aqueous Milieu Interact with t-PlaF Primarily via Entering T3

345 Subsequently, we investigated if C10 from the aqueous milieu could directly bind to PlaF without prior
346 entry into the bilayer. To explore this, we conducted all-atom unbiased MD simulations of free ligand
347 diffusion (fldMD) of 1 μs length. Such simulations have been previously used to predict the binding
348 modes of molecules (19). t-PlaF was embedded in a bilayer with the composition DOPE:DOPG of 3:1
349 and 10 molecules of C10 were added to the water phase, resulting in concentrations of 30 mM in the
350 solvation box. This higher concentration than the experimentally used one was chosen to increase the
351 probability of observing events of C10 binding to and dissociating from t-PlaF. As this concentration is
352 above the CMC of C10 (35), we monitored by visual inspection of the trajectories that no C10 aggregates
353 formed.

354 We performed 12 replicas, and binding and unbinding events of C10 were monitored **(Figure S12)**. We
355 identified a C10 as "bound" if it is within a distance < 5 Å from the T3 entrance defined as COM of
356 residues K170, Q234, and Y236 and has an RMSD < 1.5 Å to the previous position within the trajectory
357 (see Supplementary results) (15). Density maps of C10 around t-PlaF show that C10 tends to gather in
358 T3 **(Figure 6A)**, as also supported by the finding that T3 is involved in 8.61% of the total binding events
359 of C10 to t-PlaF (**Figure S12**). In most events, the acyl chain of C10 enters T3 first (**Figure 6B**), which
360 is compatible with the mostly hydrophobic interior of T3 (15). T3 has previously been suggested to play
361 a role in the catalytic cycle by relocating substrates during catalysis (15). Thus, the identified C10-PlaF
362 interactions in T3 may influence enzyme activity. Furthermore, it has been hypothesized that FFA
363 released from the GPL may diffuse to the periplasmic space *via* T3 (15), therefore it is feasible that C10
364 may also enter PlaF *via* the same path.

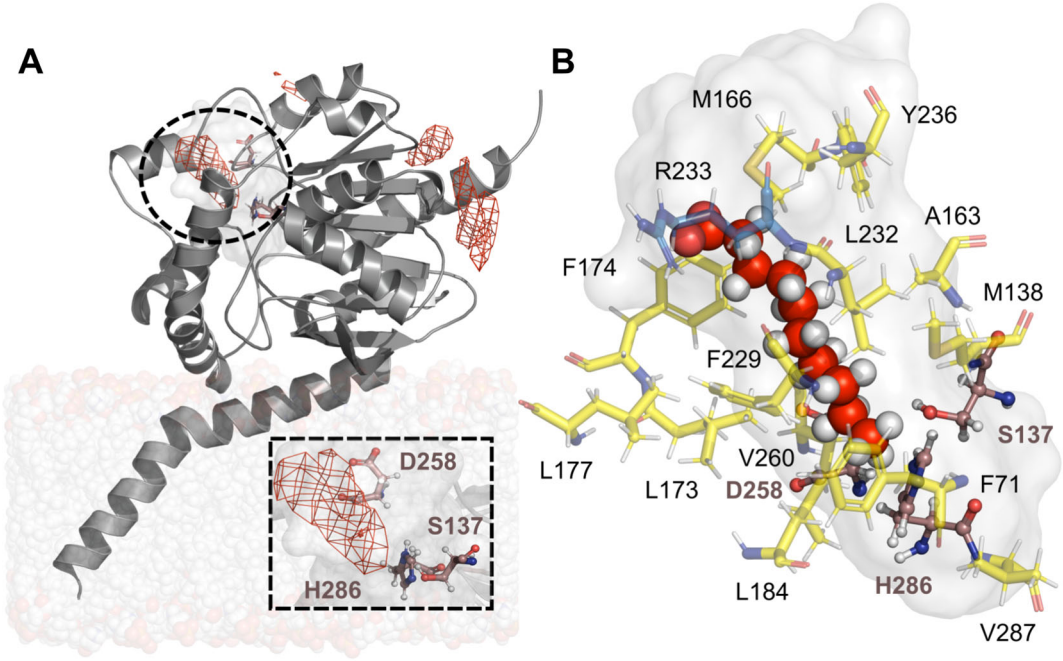

Figure 6. Free-ligand diffusion MD simulations reveal access of C10 molecules to T3. (A) 3D density grids (red mash) showing the probability density of C10 around t-PlaF. All C10 were considered in the 3D density grid calculations, and the contour level is set as one standard deviation above the mean value (1σ). T3 computed using CAVER 3.0 (36) is depicted as a light grey surface. The region (black dashed circle) around the catalytic triad (S137, D258, and H286, indicated as brown sticks) is shown in the blow-up (black dashed rectangle). **(B)** A representative binding mode of C10 located within T3 from the most populated cluster that comprises 51.8 ± 0.3% of all bound C10 configurations. T3 was calculated using CAVER 3.0 (36) and is presented as a light grey surface. Carbon and hydrogen atoms of the C10 are depicted as red and grey spheres, respectively. The catalytic triad is illustrated as brown sticks, and the T3 residues as yellow sticks, except for R233 represented as blue sticks.

2.7 Tail-first Access of C10 into T3 is Energetically Favorable

As a prerequisite to computing the energetics of binding of C10 to T3 of PlaF, we validated if C10 access *via* its tail is favorable. We applied steered MD (sMD) simulations (37) to pull C10 from the bound state obtained during fldMD simulations to the unbound state in which C10 is located outside T3 in an aqueous milieu. We did not use a trajectory from the fldMD simulations as the C10 tail did not insert deeply enough into T3 to reach the catalytic site. The transition pathway will be later used to define reference points for US simulations to compute a PMF of C10 egress. A bound C10 of replica 4 of the fldMD simulations was chosen as a representative pose (**Table S5** (t-PlaF(III): CAP-1127)). The terminal carbon atom of C10 was considered for pulling from a distance of 3.4 Å to the catalytic oxygen of S137 to 13.1 Å, where it is in the solvent. The C10 was pulled through four consecutive virtual points

386 **(Figure 7A, B)** chosen such that the entire egress pathway was covered as described before (15). The
387 distance between the pulled C-terminal carbon atom and the virtual point was used as a reaction
388 coordinate. The pulling was repeated 50 times for each step, and the work done was computed as a
389 function of the reaction coordinate, as done in previous work (15) **(Figure 7A)**. By applying Jarzynski's
390 relation (eq. 1) (38), the work was related to the free energy difference between the respective two states
391 along the transition pathway.

392 $$\overline{e^{-W/kT}} = e^{-\Delta F/kT} \quad \text{(eq. 1)}$$

393 The sMD trajectory whose work-*versus*-reaction coordinate profile is closest to the Jarzynski average
394 was identified as the most favorable transition pathway (15) **(Figure 7B).** Its endpoint provided the
395 starting point for the sMD simulations in the next part of the transition pathway. As a result, the transition
396 pathway is close to the lowest-free energy pathway of C10 egress from the catalytic site to the aqueous
397 milieu. Overall, this approach is similar to sampling unbinding trajectories of ligands from proteins
398 before applying Jarzynski's relation (39-41) but uses piecewise sMD simulations along the pathway to
399 account for the curvilinear tunnel. A total of 1.15 μs of sMD simulation time was used.

400 PMFs were computed from US simulations along the sMD-determined transition pathway (24) and post-
401 processed with WHAM (42, 43) to evaluate the energetics of C10 egress. As a reaction coordinate, the
402 distance between the terminal carbon atom of C10 to the side-chain oxygen of the catalytic S137 was
403 used. In total, 29 windows were sampled with 260 ns of sampling time each, of which the first 100 ns
404 were discarded as equilibration. The kernel density showed a median overlap of 33.6 ± 3.1% between
405 contiguous windows, well suited for PMF calculations (26). The PMF of C10 egress is converged and
406 precise **(Figure S13)**. It reveals the presence of an energetic global minimum associated with the bound
407 state I which is ~4 kcal mol^{-1} more favorable than the partially bound states II and III as well as the
408 unbound state IV (**Figure 7C, D**). The computed binding free energy (ΔG°_{comp}, (25))
409 of -3.17 ± 0.15 kcal mol^{-1} indicates that tail-first access of C10 to T3 is energetically favorable. These
410 results further strengthen the suggestion that the entry of C10 from the aqueous milieu to T3 and its

binding close to S137 could prevent a substrate (GPL or LGPL) from reaching the catalytic site, thereby competitively inhibiting PlaF activity (15).

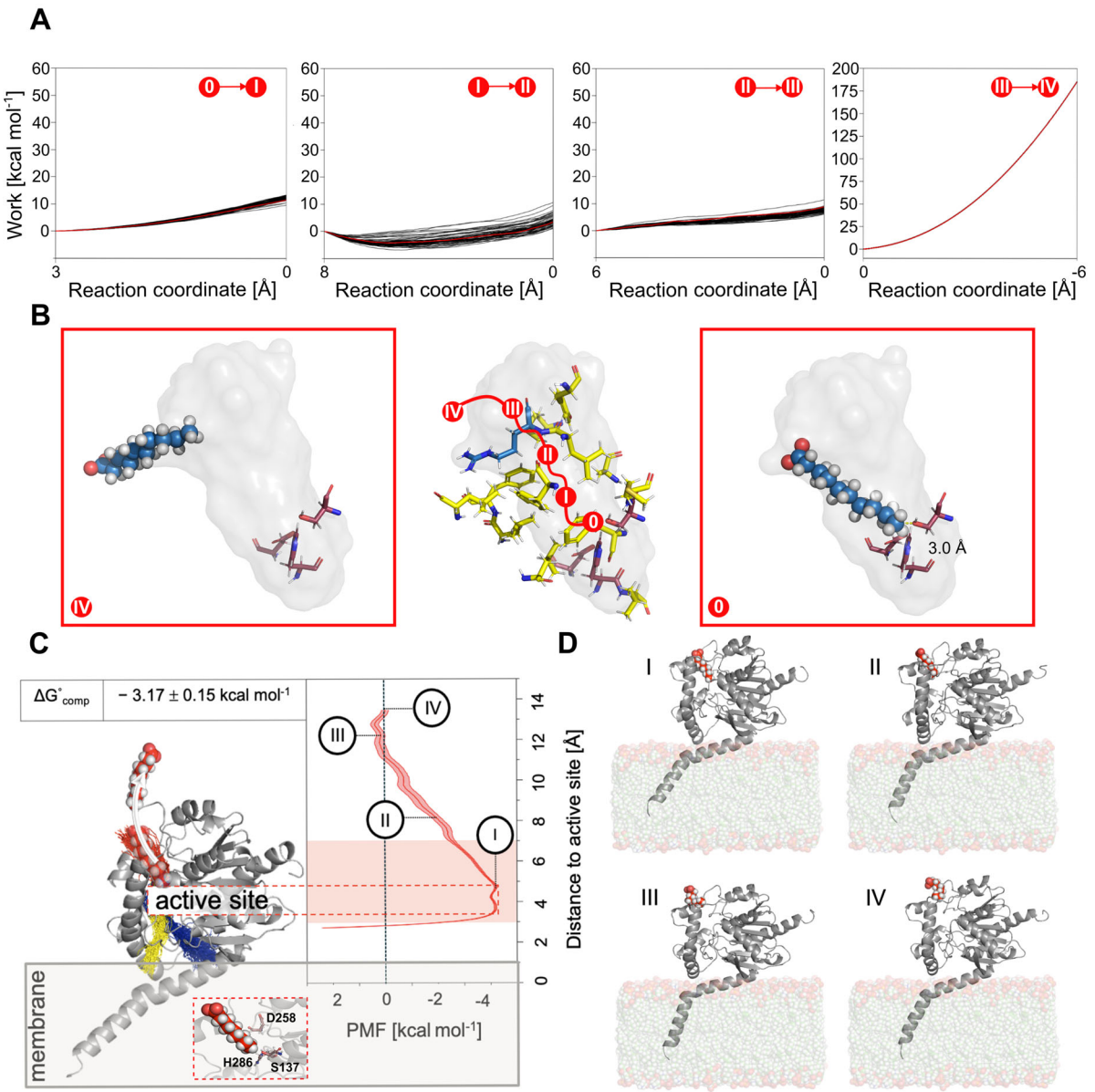

Figure 7. Binding free energy of C10 to T3 as determined by sMD and umbrella sampling. Work distributions (black lines) were obtained from 50 replicas of sMD simulations. **A)** C10 is pulled out of T3 via its tail. C10 is first pulled from the bound position (0) to point I. A replica closest to Jarzynski's average (red line) was considered as the starting point for the next pulling, I → II. This pulling continues until IV, after which C10 is completely pulled out of T3. The reaction coordinate denotes the distance to the target point. **B)** The starting point and the final point of the pulling are illustrated. (0) is the initial bound position with a distance of 3.0 Å between the catalytic Ser oxygen and the terminal methyl group of the fatty acid. (IV) is the final position, with the terminal methyl group of the fatty acid being pulled out of the tunnel. The catalytic triad residues are represented with purple sticks. The grey T3 tunnel surface was computed with CAVER 3.0 (36). PMF profile of C10 egress through T3 in the t-PlaF

424 configuration **(C)** and corresponding states **(D)**. **(C)** The entrance of T3 (red) is located > 35 Å above
425 the membrane, pointing into the aqueous milieu; T1 and T2 (blue and yellow, respectively) point to the
426 membrane. C10 is pulled from the bound state through T3 into the water phase mimicking the
427 periplasmic space in the cell. The catalytic site is marked with a dotted red box. The red-shaded area
428 around the curve represents the SEM. The red-shaded box corresponds to the integration limits used to
429 calculate K_{eq} (eq. 2) to determine ΔG°_{comp}. **(D)** Corresponding states during the C10 egress. State I:
430 Starting position of C10 (in the bound state). State II: C10 tail reaches half of the tunnel. State III: C10
431 tail is close to the tunnel interface with the periplasmic space. State IV: C10 reaches the end of the T3.
432 The C10 molecule is surrounded by water.

433 **2.8 Tryptophan Substitutions in T3 are suggested to Interfere with C10 Access**

434 To validate the prediction that T3 is the preferred pathway for C10 entering PlaF from the water phase,
435 we used the previously characterized Trp substitutions F229W and L177W within T3 that caused tunnel
436 constriction **(Table 1)** without affecting protein thermostability (15). This strategy had previously been
437 employed to block tunnels of dehalogenases (44) and PlaF (15) with respect to substrate access. T3
438 could be identified at a similar occurrence rate **(Table 1)** in $PlaF_{WT}$ and both PlaF variants, therefore
439 these Trp variants are suitable for experimentally studying the binding of C10 from the aqueous milieu
440 to the T3.

441 MD simulations of free ligand diffusion of C10 were performed to observe binding events to T3 in the
442 two PlaF variants, applying the same criteria as described for $PlaF_{WT}$. The results indicated a reduction
443 in the number of C10 binding events to T3 compared to $PlaF_{WT}$ to 6.90% in $PlaF_{F229W}$ and 5.42% in
444 $PlaF_{L177W}$ variant **(Table 1, Figures S12, S14, S15)**. 3D density grids of C10 molecules from fldMD
445 simulation trajectories indicated that the C10 occurrences around the two engineered Trp sites are
446 reduced compared to the $PlaF_{WT}$ but the orientation and the depth by which C10 immerses into T3 are
447 similar among all three proteins (**Figure 8A**).

448 To further evaluate the effect of the Trp substitutions on C10 interactions within T3, we computed
449 binding effective free energies using MM-PBSA with an implicit membrane model (45, 46). For this,
450 frames from the fldMD simulations with bound C10 were used. The computations are converged, as
451 evidenced by the comparison between the first and the second halves of the trajectories (**Figure S16)**.
452 Across 12 different replicas, we identified 24, 19, and 14 trajectories in which C10 were bound to T3 of
453 $PlaF_{WT}$, $PlaF_{F229W}$, and $PlaF_{L177W}$, respectively. The results revealed that C10 molecules bind to T3 more

454 favorably in the Trp variants (ΔG_{eff}(PlaF$_{F229W}$) = -17.90 ± 0.55 kcal mol^{-1}; ΔG_{eff}(PlaF$_{L177W}$) = -21.28 ±
455 1.51 kcal mol^{-1}) than the WT (ΔG_{eff}(PlaF$_{WT}$) = -16.47 ± 0.53 kcal mol^{-1}) **(Table 1, Figure 8A)**. Such a
456 more prevalent bound state may explain a reduced number of binding events of C10 to T3 of Trp variants
457 (**Table 1**). The more favorable binding in the variants likely arises from better interactions of the
458 lipophilic tail of C10 with the bulky sidechain of Trp than the WT residues.
459 To experimentally investigate the effect of the Trp substitutions in T3 on the inhibition of PlaF by C10,
460 we produced PlaF$_{WT}$, PlaF$_{F229W}$, and PlaF$_{L177W}$ using the *P. aeruginosa* expression system (6), purified
461 proteins in the presence of dodecyl-β-D-maltosid (DDM) using IMAC (15), and reconstituted them in
462 DOPE:DOPG SUVs using a methodology similar to that employed for LL domain variants. Subsequent
463 inhibition studies by varying concentrations of C10 while keeping the protein and substrate
464 concentrations constant revealed half-maximal inhibitory concentrations (IC_{50}) for PlaF$_{WT}$ and Trp
465 variants **(Figure 8B)**. Results show reduced IC_{50} values of Trp variants compared to the WT, indicating
466 a stronger inhibitory effect of C10 on Trp variants in comparison to the PlaF$_{WT}$. These experimental
467 results are in agreement with computed binding effective free energies **(Table 1)** and further strengthen
468 the role of T3 in the binding of C10.
469

470 **Table 1. Effect of single mutations on C10 binding to T3 in t-PlaF WT and two variants**
471 **identified from fldMD simulations.**

PlaF	Occurrence[a]	Average bottleneck radius[b,c]	C10 binding events[d]	Effective binding free energy[e]
WT	27.75	2.29 ± 0.32	8.61	-16.47 ± 0.53
F229W	24.78	1.67 ± 0.31	6.90	-17.90 ± 0.55
L177W	28.37	1.70 ± 0.34	5.42	-21.28 ± 1.51

472 [a] Frequency of occurrence of T3 in CAVER; in %.
473 [b] Data was calculated with CAVER using a probe radius of 1.2 Å.
474 [c] In Å; the average and SD are given.
475 [d] Frequency that describes the number of T3-bound frames compared to the total number of
476 frames; in %.
477 [e] In kcal mol^{-1}; the average and SEM are given.

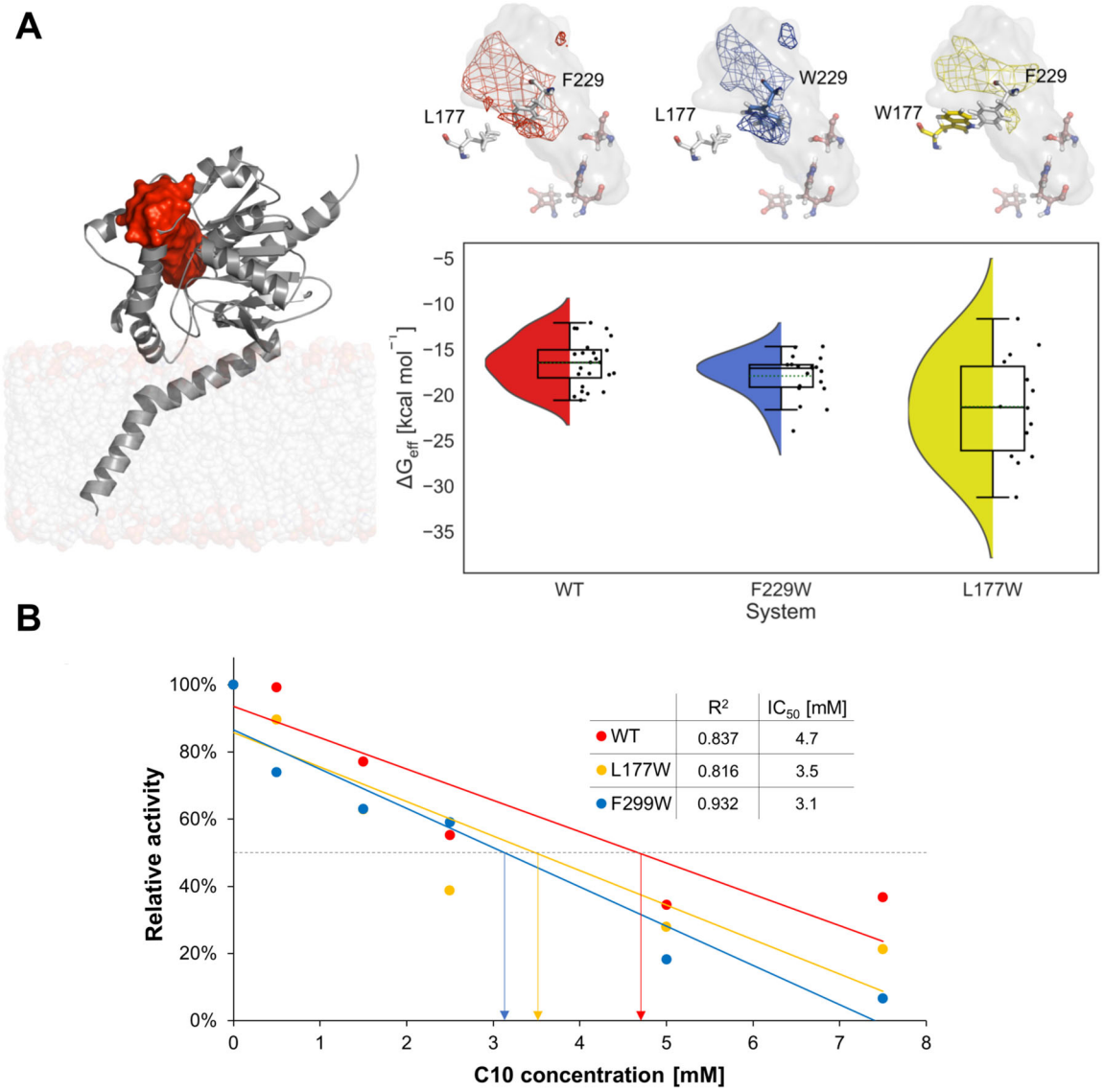

Figure 8. Effect of T3 mutations on FFA binding to PlaF. A) Binding of FFA to T3 in the $PlaF_{WT}$ and the Trp variants. Left: The $PlaF_{WT}$ T3 is shown as a red surface in t-PlaF (grey cartoon). Top-right: C10 3D density grids based on fldMD simulations are shown. The contour level is set as 1σ. T3 is depicted as a grey surface and the catalytic triad as brown sticks. The substitution sites are shown in white sticks, except for the included tryptophans, which are represented as blue sticks for $PlaF_{F229W}$ and yellow sticks for $PlaF_{L177W}$. The density grids are colored accordingly, except for the WT, which is shown in red. Bottom-right: The violin plot indicates the distribution of the binding effective energies of FFAs to T3. The inner box of a box plot represents the interquartile range, with the horizontal black line indicating the median. The dotted green line represents the mean, and the vertical black line shows the rest of the distribution, excluding points determined to be outliers when they fall outside 1.5 times the interquartile range. **B)** Inhibitory effect of C10 on $PlaF_{WT}$ and PlaF variants. Linear plots of relative activities (sample without C10 was set to 100%) and C10 at concentrations in a range of 0 – 7.5 mM. Linear correlation coefficients (R^2) and IC_{50} values are indicated. The results represent the mean of initial reaction velocities measured six times using esterase substrate (*p*-NPB) and proteins purified in the presence of DDM.

494 **3. DISCUSSION**

495 In this study, we combined molecular simulations at the atomistic level with biochemical experiments
496 to examine how the interaction of medium-chain FFAs with PlaF regulates PlaF activity. Using *in vivo*,
497 *in vitro*, and computational analyses, we previously established a model (6) according to which
498 homodimerization of catalytically active PlaF monomers leads to PlaF inhibition, a process induced by
499 medium chain (C10 - C14) FFAs. Following monomerization, PlaF reorients in the bilayer by tilting,
500 (6) which is essential for its activation as it allows membrane-bound GPL substrates to reach the active
501 site (15). Here, we further refined the model of PlaF activity regulation by assessing the impact of C10
502 located (i) in the GPL bilayer or (ii) in the aqueous milieu surrounding the GPL bilayer on the dimer-
503 monomer transition and the tilting as well as on substrate access to the active site.

504 *i) Effect of FFAs in the GPL bilayer on PlaF.*

505 Our MD simulations and PMF computations revealed that C10 in the GPL bilayer exerts a stabilizing
506 effect on the inactive di-PlaF configuration, in accordance with findings from covalent crosslinking
507 experiments (6). This stabilization likely arises from favorable interactions between FFAs localized in
508 the upper bilayer leaflet and predominantly positively charged residues located in PlaF's LL domain,
509 which is close to the upper leaflet in the di-PlaF configuration. Mutagenesis experiments and DMP-
510 crosslinking studies using purified proteins functionally validated the predictions by showing that
511 single-charged residue-to-alanine variants exhibited a reduced dimerization compared to $PlaF_{WT}$.
512 Notably, higher C10 concentrations were predicted to stabilize di-PlaF more, which led us to
513 hypothesize that multiple interactions between membrane-localized FFAs and residues within the LL
514 domain occur simultaneously. We validated this hypothesis by using double variants carrying
515 combinations of residues identified as FFA interaction sites in our MD simulations. These double
516 variants showed a more strongly reduced PlaF dimerization than single-point variants. Furthermore, our
517 MD simulations and PMF computations indicated that C10 promotes the t-PlaF configuration and
518 facilitates the tilting process. The latter might be attributed to a potential reduction in membrane
519 viscosity caused by the addition of FFAs as membrane components (47). Still, considering physiological

520 conditions in the *P. aeruginosa* WT and that the equilibria for dimer-to-monomer transition and tilting
521 are coupled, between 2.3 and 7.3% of the PlaF molecules are predicted to be in a monomeric, tilted,
522 catalytically active state in *P. aeruginosa* when 20 mol% C10 are present in the upper leaflet. This is
523 more than 10-fold less than in *P. aeruginosa* WT in the absence of C10 (6). The observed impact of
524 FFAs located in the GPL bilayer on the transitions of PlaF likely contributes to the non-
525 competitive/allosteric component of a mixed inhibition kinetics mechanism previously demonstrated for
526 FFA acting on PlaF (6).

527 *ii) Effect of FFAs in aqueous milieu on PlaF.*

528 Medium-chain FFAs were cocrystallized in the active site of PlaF, and they compete with the substrate
529 according to previous inhibition kinetics results (6). To scrutinize if C10 localized in the water phase of
530 a bilayer-bound PlaF can interact with the enzyme such that substrate binding is impacted, we performed
531 fldMD simulations. These simulations revealed that C10 can bind to the active monomeric t-PlaF *via*
532 T3, which was previously identified to connect the active site of PlaF with the surrounding water milieu
533 (15). C10 favors tail-first access and can reach close to the catalytic triad with its tail. In such a
534 configuration, C10 may potentially interfere with substrate binding, which could explain the
535 experimentally determined competitive effect of C10 on PlaF. We next studied by fldMD simulations
536 previously characterized PlaF variants with genetically engineered bulky Trp residues in T3 ($PlaF_{F229W}$
537 or $PlaF_{L177W}$) (15). The simulations revealed that binding events for C10 occurred less frequently in
538 either single variant, as might have been expected due to the narrowed T3. Interestingly, binding
539 effective free energy computations revealed that C10 binds stronger to T3 in the variants, i.e., the less
540 frequent binding events there result from C10 being bound longer in T3. These predictions are in line
541 with biochemical studies revealing that inhibition of the PlaF variants reconstituted in SUVs by C10
542 was enhanced compared to $PlaF_{WT}$. Together, our results indicate that T3 is involved in the inhibition of
543 PlaF by C10 in the water phase.

544 *Possible physiological relevance of FFA-mediated PlaF inhibition.*

545 Comparative GC-MS profiling of FFAs secreted by *P. aeruginosa* Δ*plaF* and the wild-type cells
546 revealed that PlaF can release medium-chain FFAs, including C10 and C14, from GPLs as *in vitro*
547 substrates. This result corroborates our suggestion that PlaF exerts multiple physiological functions (48)
548 through GPL degradation (6). We observed that the chain length of the FFAs has a minor impact on the
549 tilting transition (6), indicating that other medium-chain FFAs may influence PlaF similarly as described
550 here for C10. At physiologically relevant concentrations in *P. aeruginosa*, we estimated that PlaF
551 predominantly exists as inactive di-PlaF in the presence of FFAs. These results together with the
552 predicted function of T3 for C10 inhibition strongly suggest that product feedback regulation of PlaF
553 catalytic activity may be important for *in vivo* PlaF-mediated GPL degradation and membrane
554 remodeling.

555 In conclusion, our study provides detailed mechanistic insights into the impact of medium-chain FFAs
556 on the regulation of PlaF activity *in vitro*. While likely similar mechanisms are active *in vivo*, this needs
557 to be experimentally validated in the future. Disentangling FFA-mediated activity regulation of the
558 integral membrane protein PlaF is challenging as FFAs may bind into the protein, interact with the
559 protein from the bilayer, and change bilayer properties (e.g., viscosity). Our MD simulations and free
560 energy computations provide evidence that the interplay of these mechanisms serves as a regulatory
561 factor governing PlaF function. Studying membrane proteins in near-native conditions within GPL
562 vesicles as done here shall help to disentangle these complex relationships further. Our results should
563 help understand the regulatory role of FFAs present in the periplasm or inner bacterial membrane on
564 PlaF and eventually other single TM helix spanning membrane proteins because FFAs are among the
565 most common regulators of protein function (49). They also open up new perspectives on how to inhibit
566 PlaF, which has been suggested as a promising target for developing new antibiotics against *P.*
567 *aeruginosa* (6).

568 # 4 MATERIALS AND METHODS

569 ## 4.1 Gas Chromatography-mass Spectrometric (GC-MS) Analysis of FAs Extracted from *P.*
570 *aeruginosa*

571 *P. aeruginosa* PA01 (wild-type, WT) and the Δ*plaF* mutant were cultivated overnight (37 ℃, LB
572 medium, agitation), and cells were separated from the supernatant, followed by chloroform/methanol
573 extraction of FFAs, derivatization of FFAs with *N*-methyl-N-(trimethylsilyl) trifluoroacetamide, and
574 quantification by GC-MS as described in ref. (50).

575 ## 4.2 Preparation of Starting Structures

576 The crystal structure of the PlaF dimer is available in the Protein Data Bank (PDB ID 6I8W) (51). The
577 last five residues of the C-terminus of each monomer missing in the structure were added using
578 MODELLER (52), and all small molecule ligands were removed. The dimer was oriented in the
579 membrane using the PPM server (di-PlaF) (22). From that, the "split" s-PlaF$_A$ configuration of chain A
580 was generated by removing chain B from the dimer orientation. Additionally, chain A was oriented
581 using the PPM server, resulting in the tilted configuration t-PlaF. These three starting configurations,
582 di-PlaF, s-PlaF, and t-PlaF, were embedded into a DOPE:DOPG = 3:1 membrane (53) and solvated
583 using PACKMOL-Memgen (54, 55). The membrane composition resembles that of the native inner
584 membrane of Gram-negative bacteria (53).
585 Free fatty acids (FFA) of different chain lengths were added as upper-leaflet components in the
586 protonated form (56) in two different concentrations; here, "upper" refers to the leaflet pointing to the
587 periplasmic space. A distance of at least 15 Å between the protein or membrane and the solvent box
588 boundaries was kept. To obtain a neutral system, counter ions were added that replaced solvent
589 molecules (KCl 0.15 M). The generated systems are summarized in **Table S3**. The size of the resulting
590 systems was ∼140,000 atoms for s-PlaF and t-PlaF and ∼185,000 atoms for di-PlaF.

591 ## 4.3 Unbiased Molecular Dynamics Simulations of PlaF Monomers

592 The GPU particle mesh Ewald implementation from the AMBER21 suite of molecular simulation
593 programs (57) with the ff14SB (58) and Lipid14/17 forcefields (59, 60) for the protein and the membrane
594 lipids, respectively, were used; water molecules and ions were parametrized using the TIP3P model (61)
595 and the Li and Merz 12-6 ions parameters (62, 63). For the monomer configurations (s-PlaF and t-PlaF),
596 12 independent simulations of 1 μs length were performed (**Table S3**). Covalent bonds to hydrogens
597 were constrained with the SHAKE algorithm (64) in all simulations, allowing the use of a time step of
598 2 fs. Details of the thermalization of the simulation systems are given below. All unbiased MD
599 simulations showed stable protein structures and membrane phases evidenced by electron density
600 calculations (**Table S3, Figures S2-S5**).

601 4.4 Relaxation, Thermalization, and Production Runs of the PlaF Monomers.

602 An initial minimization step was performed with the CPU code of pmemd (65). Each minimization was
603 organized in four steps of 1000 cycles each, for a total of 4000 cycles of minimization. Afterward, each
604 minimized system was thermalized in one stage from 0 to 300 K over 25 ps using the NVT ensemble
605 and the Langevin thermostat (66), and the density was adapted to 1.0 g cm^{-3} over 975 ps using the NPT
606 ensemble with a semi-isotropic Berendsen barostat (67) with the pressure set to 1 bar. The thermalization
607 and equilibration were performed with the GPU code of pmemd (65). There are three density
608 equilibration steps with a total time of 4 ns. The sum of thermalization, density adaptation, and
609 equilibration takes 5 ns.
610 For each replica, 1 μs of production run using the GPU code of pmemd was performed in the NPT
611 ensemble at a temperature of 300 K using the Langevin thermostat (66) and a collision frequency of
612 1 ps^{-1}. To avoid noticeable distortions in the simulation box size, semi-isotropic pressure scaling using
613 the Berendsen barostat (67) and a pressure relaxation time of 1 ps was employed by coupling the box
614 size changes along the membrane plane (68).

615 4.5 Analysis of MD Trajectories of the PlaF Monomer

616 The trajectories were analyzed with CPPTRAJ (33). As in ref. (6), the angle between the membrane
617 normal and the vector between the COM of Cα atoms of residues 21–25 and residues 35–38 was
618 calculated to describe the tilting of monomeric PlaF.

619 4.6 PMF and Free Energy Calculation of Dimer Dissociation

620 For calculating a configurational free energy profile (PMF) of dimer separation, 71 intermediate states
621 were generated by separating one chain of the dimer along the membrane plane in steps of 0.5 Å,
622 respectively. The generated structures represent the separation process of the PlaF dimer. To sample
623 configurations along the chain separation in a membrane environment, each intermediate state was
624 embedded into a membrane of approximately 157x157 Å by using PACKMOL-Memgen (55) (see
625 chapter 4.2 and **Table S3** for the composition of the systems). Each intermediate state was minimized,
626 thermalized, and equilibrated following the protocol already described (sections 4.2 and 4.3).
627 Umbrella sampling simulations were performed starting from each equilibrated intermediate state by
628 restraining the initial distance between chains in every window with a harmonic potential, using a force
629 constant of 4 kcal mol^{-1} $Å^{-2}$ (24); the distance between the COM of C_α atoms of residues 25-38 of each
630 monomer was used as a reaction coordinate value *r*. Independent MD simulations of 800 ns in length
631 each were started from each intermediate state, resulting in a total simulation time of 56.8 μs. *r* was
632 recorded every 2 ps and post-processed with the Weighted Histogram Analysis Method implementation
633 of A. Grossfield (WHAM 2.0.9)(42), removing the first 640 ns as an equilibration phase of the system.
634 The error was estimated by considering the last 160 ns only and by calculating the standard error of the
635 mean from eight independent free energy profiles determined every 20 ns during this time. The overlap
636 between contiguous windows and the convergence of the PMFs was validated **(Figures S8-9)**. The
637 association free energy was estimated from the obtained PMF following the membrane two-body
638 derivation (28) and our previous work (6, 27) (eqs. S1-4).

639 4.7 PMF and Free Energy Calculation of Monomer Tilting

640 The initial conformations used in every window for calculating the PMF of the monomer tilting were
641 obtained from the first microsecond of MD simulations of replica 2 of s-PlaF in the Tilt1 system **(Table**

642 **S3).** Oriented as in the di-PlaF crystal structure, the monomer spontaneously tilted. The distance *d* along
643 the z-axis between the COM of C_α atoms of residues 33-37 of the monomer with the membrane center
644 was used to select 40 intermediate tilting configurations as done already with a standard membrane
645 composition (6). The starting conformations were extracted from the representative trajectory, taking
646 the respective snapshots where *d* showed the least absolute deviation to the average value obtained by
647 binning *d* in windows of 0.5 Å width and with an evenly distributed separation of 0.5 Å. *d* was restrained
648 for every configuration by a harmonic potential with a force constant of 4 kcal mol^{-1} $Å^{-2}$, and sampling
649 was performed for 800 ns per window. *d* values were obtained every 2 ps and analyzed as described
650 above. The error was estimated in the same way as for the dimerization. The overlap between contiguous
651 windows and the convergence of the PMF was validated **(Figure S7)**. The free energy of monomer
652 tilting was estimated from the obtained PMF following protocols explained in previous works (6, 25)
653 (eqs. S5-6).
654 The dissociation and tilting equilibrium constants as well as the proportion of PlaF dimer versus
655 monomer in a live cell of *P. aeruginosa* were calculated in the same way as in ref. (6); see also the
656 Supplementary Information.

657 4.8 Density Maps of Free Fatty Acids Binding to di-PlaF in the Membrane

658 The structure of the PlaF dimer was embedded in a phospholipid membrane with the composition
659 DOPE:DOPG 3:1 following the protocol described in section 4.1. C10 fatty acids were added as
660 membrane upper leaflet components in the protonated configuration (56). The final composition of the
661 upper leaflet is DOPE:DOPG:C10 3:1:1. Unbiased MD simulations of the system were performed
662 following the protocol used for the monomers (see sections 4.2 and 4.3). From the obtained trajectories,
663 all FFA binding poses were identified in which FFAs have an RMSD < 1.5 Å to the previous frame (see
664 Supplementary results), and are located at most 5 Å away from the protein. These binding poses were
665 clustered using the hierarchical agglomerative (bottom-up) algorithm implemented in cpptraj (33), using
666 the minimum distance ε between the clusters as the cluster criterion. Starting from ε = 2.0 Å, we
667 gradually increased ε in 0.5 Å intervals until the population of the largest cluster remained unchanged,
668 (ε = 5.0 Å). We calculated the 3D density maps of the fatty acids considering all atoms using the grid

669 function available in CPPTRAJ, using a grid spacing of 1.5 Å (33). We applied a contour level of 1σ
670 (one standard deviation above the mean value).

671 4.9 fldMD to study C10 FFA Binding from the Water Phase to t-PlaF

672 t-PlaF was embedded in a phospholipid membrane with the composition DOPE:DOPG = 3:1 following
673 the protocol described in section 4.1. To investigate the binding of FFAs to PlaF, 1 μs long MD
674 simulations of the free diffusion of FFA molecules located in the water phase were performed to
675 investigate their binding to t-PlaF. The FFAs were assumed to be in their deprotonated configuration,
676 resulting in a concentration of ~30 mM in the corresponding solvation box. The eventual formation of
677 aggregates was checked by visual inspection of the trajectories. 12 replicas of 1 μs simulation length
678 were run for each system. The minimization, thermalization, equilibration, and production schemes are
679 like the ones performed in sections 4.2 and 4.3.

680 4.10 Simulated Extraction of Fatty Acids through T3

681 MD simulations were performed using the GPU implementation of the AMBER 21 molecular
682 simulation package (55), employing the same protocol as in chapters 4.3 and 4.4. To extract an FFA
683 from T3 into the periplasmic space, we selected a bound FFA (**Table S3** (t-PlaF(III): CAP-1127)) of
684 replica 4 of the fldMD simulations as a representative pose. We pulled it by its terminal carbon atom
685 from the catalytic center to the tunnel's exit using constant velocity sMD simulations, with a constant
686 velocity of 1 Å ns^{-1} and a force constant of 5 kcal mol^{-1} $Å^{-2}$ (37, 41). Pulling simulations at low velocities
687 have been used with lipids to calculate free energy profiles (15, 69). Using low pulling rates, the lipids
688 have time to adapt to energetically favorable conformations during the extraction process. T3 was
689 divided into consecutive fragments connected to T3 pulling points generated by the COM of specific
690 amino acid residues (**Table S5**). We performed 50 replicas for each pulling simulation to identify the
691 lowest energy pathway. The work was computed as a function of the reaction coordinate. The computed
692 work was further related to the free energy difference between two states of the pulling simulation by
693 applying Jarzynski's relation (eq. 1) (38). ΔF is the free energy difference between two states, which is
694 connected to the work W done on the system. k is the Boltzmann constant, and T is the absolute

temperature of the system. The replica closest to Jarzynski's average (38) was considered to describe the lowest free energy pathway, and provided the starting point for the next pulling stage, as done in ref. (15). This procedure results in faster convergence of PMF profiles subsequently computed along the pathway, decreasing the overall computations needed (39).

4.11 Umbrella Sampling Simulations and PMF calculations

To understand the energetic contribution associated with the binding of C10 molecules to T3, PMFs were computed based on umbrella sampling, taking structures from the sMD simulations (see chapter 4.10) as starting points. As a reaction coordinate, the distance of the terminal carbon atom of the FFA to the hydroxyl oxygen of S137 of the active site was used. Consecutive positions of the FFA from the bound state to the periplasmic space, as determined in chapter 4.10, were considered reference points, defining the umbrella windows. To achieve sufficient overlap between the umbrella windows, distances between reference points of 0.5 Å were used. The length of T3 and the size of the FFA can vary. Therefore, for sampling the egress of the bound fatty acid, different numbers of windows were required for the tunnel. The FFA was restrained by harmonic potentials to the reference points, using a force constant of 5 kcal mol^{-1} $Å^{-2}$. To achieve sufficient convergence of the PMF profile **(Figure S14)**, each window was sampled for 260 ns, of which the last 160 ns were used to calculate the PMF. Distance values were recorded every 2 ps and processed with WHAM (42). The PMFs were evaluated for convergence by checking the change in the free energy profile with increasing sampling time in steps of 20 ns **(Figure S14)**.

4.12 Absolute Binding Free Energy from the PMF

The absolute binding free energy of fatty acids to PlaF was determined from the computed PMF using an approach modified (15) from Chen and Kuyucak (26). The PMF was integrated along the reaction coordinate (eq. 2) to calculate an association (equilibrium) constant (K_{eq}).

$$K_{eq} = \pi r^2 \int_{periplasm}^{active_site} e^{-W(\xi)/k_B T}\, d\xi \qquad (2)$$

719 Here, r is the maximum bottleneck radius of the respective tunnel, which was determined by CAVER
720 analysis (15, 36), πr^2 is the maximum cross-sectional area of the tunnel, $W(\xi)$ is the PMF at a specific
721 value of the reaction coordinate, k is the Boltzmann constant, and T is the absolute temperature at which
722 the simulations were performed. The integration limits describe the bound state. A reaction coordinate
723 > 7 Å was considered as an unbound state and for this reason not included in the integration.

724 K_{eq} was then transformed to the mole fraction scale (K_x). For (un)binding to the solution, a standard state
725 of 1 M is considered (25) (eq. 3).

726 $$K_x = K_{eq} \frac{1\,mol}{1\,l} = K_{eq} \frac{1}{1660\,\text{Å}^3} \quad (3)$$

727 From K_x, the difference in the standard free energy (eq. 4) between the bound and unbound states
728 (ΔG_{comp}°) of a single substrate molecule was calculated.

729 $$\Delta G_{comp}^{\circ} = -RTln(K_x) \quad (4)$$

730 4.13 Predicting Mutations to Modify Access of the Free Fatty Acid to T3

731 To verify the prediction that FFA can bind to T3 and, thereby, inhibit PlaF, we intended to alter the
732 geometry of T3 by introducing small-to-tryptophan substitutions of tunnel-lining residues, following an
733 approach already pursued (15). The selected residues were substituted to tryptophan using FoldX (70),
734 and the stability of the PlaF variants was evaluated in terms of the change in folding free energy ($\Delta\Delta G$)
735 with respect to the wild-type (71) **(Table S6)**. Single and double amino acid substitutions were
736 performed 10 times for each residue or residue couple, and the results were averaged. If the average
737 $\Delta\Delta G$ > 3 kcal mol^{-1}, the substitution is considered destabilizing (72) and was not further pursued. To
738 check if the proposed substitutions will modify the tunnel geometry, the bottleneck radius and the tunnel
739 length of the variant tunnels were calculated using CAVER 3.0 (36) **(Table S6)**. The COM of the
740 catalytic residues S137 and H286 were defined as the starting points of the search, as done in our
741 previous work (15). The probe radius was set to 1.2 Å.
742 Mutant fldMD simulations and binding free energy calculations of C10 to T3 were performed by
743 following the same protocols described for the wild-type PlaF.

744 4.14 MM-PBSA Calculations of Free Fatty Acid Binding to t-PlaF from the Water Phase

745 To pinpoint the most likely binding epitopes, we generated 3D density grids to map the location of each
746 fatty acid. Conformations stably bound (as defined in chapter 4.8) were then clustered to extract the
747 most representative binding poses. Subsequently, we conducted MM-PBSA (Molecular Mechanics-
748 Poisson Boltzmann Surface Area) calculations to determine the binding effective energy of FFAs
749 binding to t-PlaF from the water phase. These calculations were performed for both the WT PlaF and
750 the proposed mutants, utilizing the trajectories from fldMD. FFA binding poses were identified as those
751 exhibiting an RMSD < 1.5 Å compared to the previous frame (as described in chapter 2.5). Additionally,
752 these poses were required to be located within 5 Å of the entrance of T3.
753 To compute the average binding effective energy of each FFA interacting with t-PlaF within the
754 ensemble of C10 frames, we employed MMPBSA.py (46). This was done using dielectric constants of
755 1.0 for the protein, 80.0 for the solvent, and 15.0 for the membrane (73). A heterogeneous dielectric
756 model was used to represent the membrane; the implicit membrane model using spline fitting (memopt
757 = 3) was employed for these calculations (45).

758 4.15 Cloning, Site-Directed Mutagenesis, Expression, and Purification

759 Molecular biology methods were performed following previously described procedures (6). For
760 obtaining PlaF variants of the lid-like domain, site-directed mutagenesis of *plaF* (*pa2949*) was carried
761 out using the Quik-Change PCR method, with the Pfu DNA polymerase and the pET_*pa2949* plasmid
762 (74). Similarly, mutants located in the T3 tunnel were generated through site-directed mutagenesis on
763 pBBR1MCS-3_pa2949 (29). Successful site-directed mutagenesis was confirmed by DNA sequencing.
764 For the production of PlaF and the lid-like domain variants, *E. coli* BL21(DE3) cells transformed with
765 the respective expression vectors were grown overnight at 37°C in lysogeny broth (LB) medium (75)
766 supplemented with ampicillin (100 µg/ml) (74). These cultures were used to inoculate an expression
767 culture in "autoinduction" medium (terrific broth medium containing 0.04% lactose (w/v) and 0.2%
768 glucose (v/v)) supplemented with ampicillin (100 µg/ml) to an initial OD_{600nm} = 0.01. The cultures were
769 then grown for 24 h at 37 °C and harvested by centrifugation at 6750×*g* and 4 °C for 15 min.

770 For the production of PlaF and T3 tunnel variants, transformed *P. aeruginosa* PA01 cells were grown
771 overnight at 37°C in LB medium supplemented with tetracycline (100 µg/ml) (6). These cultures were
772 used to inoculate an expression culture in LB medium supplemented with tetracycline (100 µg/ml) to
773 an initial OD_{600nm} = 0.05. The cultures were grown at 37 °C until reaching OD = 2, and then harvested
774 by centrifugation at 6750×*g* and 4 °C for 15 min.
775 The total membrane fraction isolated by ultracentrifugation was solubilized with Triton X-100 (6) and
776 proteins were purified using Ni-NTA IMAC and buffers supplemented with 20 mM OG for lid-like
777 protein variants and 0.25 mM DDM for T3 tunnel protein variants. For biochemical analysis, the proteins
778 were transferred to Tris-HCl buffer (100 mM, pH 8) supplemented with the respective detergents. The
779 PlaF protein and its variants were analyzed by sodium dodecyl sulfate-polyacrylamide gel
780 electrophoresis (SDS-PAGE) under denaturation conditions on a 12 % (v/v) gel (76).

781 4.16 Reconstitution of Proteins into GPL SUVs

782 Small unilamellar vesicles (SUV) were constructed and used for reconstitution according to a modified
783 protocol (77). The GPLs used, 1,2-dioleoyl-*sn*-glycero-3-phosphoglycerol (DOPG) and 1,2-dioleoyl-
784 *sn*-glycero-3-phosphoethanolamine (DOPE), were dissolved in chloroform (Avanti Polar Lipids,
785 Alabaster, USA).
786 To produce 2.6 µmol SUVs for protein reconstitution and 64.9 µmol SUVs for fatty acid reconstitution,
787 DOPE and DOPG were mixed in a 1:1 ratio in a glass reaction vessel. The GPLs were dried under a
788 gentle stream of nitrogen and by centrifugation under a vacuum for 20 min. Subsequently, HEPES buffer
789 (20 mM, pH 8, 100 mM NaCl) was added to the dried GPLs and incubated for 10 min at room
790 temperature. The GPLs were then vortexed and sonicated for 2 min. OG and DDM were added to the
791 SUVs at a detergent:SUV ratio of 2:1 or 1:1 (mol/mol) to destabilize the SUVs, respectively. After
792 destabilization of SUVs, samples were incubated with rotation for 1 h to ensure complete equilibration
793 of the detergent with the lipids.
794 FAs were mixed with the respective detergent-destabilized SUVs to achieve a GPL-to-FA ratio of 5:1
795 (mol/mol). Proteins were mixed with the respective detergent-destabilized SUVs, with or without C10
796 to achieve a GPL-to-protein mass ratio of 20:1. Final protein concentration were 1000 nM to achieve

797 dimerization. To remove detergent, approximately 20 activated polystyrene Bio-Beads were added to
798 the reconstitution solution and incubated for 1 h with rotation at room temperature.

799 4.17 Cross-Linking Assays

800 *In vitro* cross-linking using the bifunctional cross-linking reagent dimethyl pimelimidate (DMP) was
801 performed as previously described (6). Briefly, 30 µl of proteins reconstituted into SUVs were incubated
802 with 1.8 µl of decanoic acid (332 mM) and 18 µl of freshly prepared DMP in phosphate buffer saline
803 (pH 7.4, 150 mM) for 2 h at room temperature to ensure partitioning of C10 to the bilayer. The cross-
804 linking reaction was terminated with 15 µl of stop solution (50 mM Tris-HCl, 1 M glycine, 150 mM
805 NaCl, pH 8.3).

806 4.18 Enzyme Activity Assay

807 The esterase activities of SUV-reconstituted PlaF and T3 variants were determined at 37 °C, using *p*-
808 nitrophenyl butyrate (*p*-NPB) as a substrate, following the protocol previously described (78). The
809 protein (5 µl) was mixed with 93 µl of freshly prepared 1 mM *p*-NPB solution and 2 µl of C10 dissolved
810 in DMSO. Final protein concentration were 130.22 nM, 280.52 nM, 77.22 nM for $PlaF_{WT}$, $PlaF_{L177W}$,
811 $PlaF_{F299W}$, respectively, and final FA concentrations were 0.5, 1.5, 2.5, 5, and 7.5 mM. Activities were
812 determined by measuring the release of *p*-nitrophenol spectrophotometrically during 1 h at 410 nm.
813 Inhibition was assessed by calculating the relative activities of the inhibited samples in comparison to
814 the activity of the sample without C10, which was set to 100%. IC_{50} values were estimated from linear
815 plots as done in ref. (79).

816 4.19 Thermal Stability

817 PlaF and variants loaded into the measuring capillaries (Prometheus NT.Plex nanoDSF Grade Standard
818 Capillary Chips) were heated from 20 to 90 °C (1 °C/min, heating rate), and the intrinsic protein
819 fluorescence was recorded at 330 and 350 nm using the Prometheus NT.Plex nanoDSF device
820 (NanoTemper, Munich, Germany).

821 4.20 SDS-PAGE and Western Blotting

822 Proteins were analyzed by sodium dodecyl sulphate-polyacrylamide gel electrophoresis (SDS-PAGE)
823 under denaturation conditions on 12% (w/v) gels as described previously (74). The proteins were
824 transferred from SDS-PAGE gel to the polyvinylidene difluoride membranes by western blotting and
825 were detected using anti-His(C-term)-HRP antibodies (Invitrogen) as described previously (80).

826 4.21 Detergent quantification

827 We quantified detergent following established procedures (81). To do so, 25 µl of each protein sample,
828 50 µl 5% phenol, and 125 µl 96% sulfuric acid were pipetted in a 1.5 ml Eppendorf tube. Samples were
829 vortexed and incubated at 90°C for 5 minutes. After the samples were cooled down at room temperature,
830 150 µl were transferred to a 96-well microtiter plate and absorbance was measured at 490 nm. The
831 calibration curve was prepared with respective detergent in the same manner as the samples.
832

5 ACKNOWLEDGEMENTS

This study was funded by the Deutsche Forschungsgemeinschaft (DFG, German Research Foundation) project no. 267205415 / CRC1208 grant to F.K. and K.-E.J. (subproject A02) and H.G. (subproject A03). We thank Muttalip Caliskan (IMET, HHU Düsseldorf) for help with fatty acid quantification. We are grateful for computational support by the "Zentrum für Informations und Medientechnologie" at the Heinrich-Heine-Universität Düsseldorf and the computing time provided by the John von Neumann Institute for Computing (NIC) to H.G. on the supercomputer JUWELS at Jülich Supercomputing Centre (JSC) (user IDs: HDD18; plaf).

6 AUTHOR CONTRIBUTIONS

R.G. computational investigation, analysis, visualization; M.M., B.T. experimental investigation, analysis, visualization; S.S. supervision, analysis; K.-E.J., F.K., H.G. conceptualization, supervision, analysis, funding, resources, project management. The manuscript was written with the contributions of all authors. All authors have given approval for the final version of the manuscript.

7 CONFLICT OF INTEREST STATEMENT

The authors declare no conflicts of interest.

REFERENCES

1. Gellatly SL, Bains M, Breidenstein EBM, Strehmel J, Reffuveille F, Taylor PK, et al. Novel roles for two-component regulatory systems in cytotoxicity and virulence-related properties in *Pseudomonas aeruginosa*. AIMS Microbiol. 2018;4(1):173-91.
2. Gellatly SL, Hancock RE. *Pseudomonas aeruginosa*: new insights into pathogenesis and host defenses. Pathog. Dis. 2013;67(3):159-73.
3. Hauser AR. *Pseudomonas aeruginosa*: so many virulence factors, so little time. Crit. Care Med. 2011;39(9):2193-4.
4. Flores-Diaz M, Monturiol-Gross L, Naylor C, Alape-Giron A, Flieger A. Bacterial sphingomyelinases and phospholipases as virulence factors. Microbiol. Mol. Biol. Rev. 2016;80(3):597-628.
5. Hurley BP, McCormick BA. Multiple roles of phospholipase A2 during lung infection and inflammation. Infect. Immun. 2008;76(6):2259-72.
6. Bleffert F, Granzin J, Caliskan M, Schott-Verdugo SN, Siebers M, Thiele B, et al. Structural, mechanistic, and physiological insights into phospholipase A-mediated membrane phospholipid degradation in *Pseudomonas aeruginosa*. Elife. 2022;11.
7. Chwastek G, Surma MA, Rizk S, Grosser D, Lavrynenko O, Rucinska M, et al. Principles of membrane adaptation revealed through environmentally induced bacterial lipidome remodeling. Cell. Rep. 2020;32(12):108165.
8. Hishikawa D, Hashidate T, Shimizu T, Shindou H. Diversity and function of membrane glycerophospholipids generated by the remodeling pathway in mammalian cells. J Lipid Res. 2014;55(5):799-807.
9. Benamara H, Rihouey C, Abbes I, Ben Mlouka MA, Hardouin J, Jouenne T, et al. Characterization of membrane lipidome changes in *Pseudomonas aeruginosa* during biofilm growth on glass wool. PLoS One. 2014;9(9):e108478.
10. Fernandez-Pinar R, Espinosa-Urgel M, Dubern JF, Heeb S, Ramos JL, Camara M. Fatty acid-mediated signalling between two *Pseudomonas* species. Environ. Microbiol. Rep. 2012;4(4):417-23.
11. Dulcey CE, Dekimpe V, Fauvelle DA, Milot S, Groleau MC, Doucet N, et al. The end of an old hypothesis: the *Pseudomonas* signaling molecules 4-hydroxy-2-alkylquinolines derive from fatty acids, not 3-ketofatty acids. Chem. Biol. 2013;20(12):1481-91.
12. Martinez E, Orihuela CJ, Campos-Gomez J. *Pseudomonas aeruginosa* Secretes the Oxylipin Autoinducer Synthases OdsA and OdsB via the Xcp Type 2 Secretion System. J. Bacteriol. 2022;204(7):e0011422.
13. Liu L, Li T, Cheng XJ, Peng CT, Li CC, He LH, et al. Structural and functional studies on *Pseudomonas aeruginosa* DspI: implications for its role in DSF biosynthesis. Sci. Rep. 2018;8(1):3928.
14. Songer JG. Bacterial phospholipases and their role in virulence. Trends Microbiol. 1997;5(4):156-61.
15. Ahmad S, Strunk CH, Schott-Verdugo SN, Jaeger KE, Kovacic F, Gohlke H. Substrate access mechanism in a novel membrane-bound phospholipase A of *Pseudomonas aeruginosa* concordant with specificity and regioselectivity. J. Chem. Inf. Model. 2021;61(11):5626-43.
16. Chipot C. Free energy calculations applied to membrane proteins. Methods Mol. Biol. 2008;443:121-44.
17. Lotz SD, Dickson A. Unbiased molecular dynamics of 11 min timescale drug unbinding reveals transition state stabilizing interactions. J. Am. Chem. Soc. 2018;140(2):618-28.
18. Monje-Galvan V, Warburton L, Klauda JB. Setting up all-atom molecular dynamics simulations to study the interactions of peripheral membrane proteins with model lipid bilayers. Methods Mol. Biol. 2019;1949:325-39.
19. Frieg B, Gremer L, Heise H, Willbold D, Gohlke H. Binding modes of thioflavin T and congo red to the fibril structure of amyloid-beta(1-42). Chem. Commun. (Camb). 2020;56(55):7589-92.
20. Salvador López JM, Van Bogaert INA. Microbial fatty acid transport proteins and their biotechnological potential. Biotechnol. Bioeng. 2021;118(6):2184-201.
21. Zhang YM, Rock CO. Membrane lipid homeostasis in bacteria. Nat. Rev. Microbiol. 2008;6(3):222-33.
22. Lomize MA, Pogozheva ID, Joo H, Mosberg HI, Lomize AL. OPM database and PPM web server: resources for positioning of proteins in membranes. Nucleic Acids Res. 2012;40(Database issue):D370-6.
23. Lomize MA, Lomize AL, Pogozheva ID, Mosberg HI. OPM: orientations of proteins in membranes database. Bioinformatics. 2006;22(5):623-5.
24. G.M. Torrie JPV. Nonphysical sampling distributions in Monte Carlo free-energy estimation: Umbrella sampling. J. Comput. Phys. 1977;23(2):187-99.
25. Doudou S, Burton NA, Henchman RH. Standard free energy of binding from a one-dimensional potential of mean force. J. Chem. Theory Comput. 2009;5(4):909-18.
26. Chen PC, Kuyucak S. Accurate determination of the binding free energy for KcsA-charybdotoxin complex from the potential of mean force calculations with restraints. Biophys J. 2011;100(10):2466-74.
27. Pagani G, Gohlke H. On the contributing role of the transmembrane domain for subunit-specific sensitivity of integrin activation. Sci. Rep. 2018;8(1):5733.

28. Johnston JM, Wang H, Provasi D, Filizola M. Assessing the relative stability of dimer interfaces in g protein-coupled receptors. PLoS Comput. Biol. 2012;8(8):e1002649.
29. Bleffert F, Granzin J, Gohlke H, Batra-Safferling R, Jaeger KE, Kovacic F. *Pseudomonas aeruginosa* esterase PA2949, a bacterial homolog of the human membrane esterase ABHD6: expression, purification and crystallization. Acta Crystallogr. Sect. F Struct. Biol. 2019;75(Pt 4):270-7.
30. Teufl M, Zajc CU, Traxlmayr MW. engineering strategies to overcome the stability-function trade-off in proteins. ACS Synth Biol. 2022;11(3):1030-9.
31. Namani T, Walde P. From decanoate micelles to decanoic acid/dodecylbenzenesulfonate vesicles. Langmuir. 2005;21(14):6210-9.
32. Cooper GM. The Cell: A molecular approach. 2nd edition.: Sunderland (MA): Sinauer Associates; 2000.
33. Roe DR, Cheatham TE, 3rd. PTRAJ and CPPTRAJ: software for processing and analysis of molecular dynamics trajectory data. J. Chem. Theory Comput. 2013;9(7):3084-95.
34. Schneider CA, Rasband WS, Eliceiri KW. NIH Image to ImageJ: 25 years of image analysis. Nat. Methods. 2012;9(7):671-5.
35. Hossain MS, Berg S, Bergstrom CAS, Larsson P. Aggregation behavior of medium chain fatty acids studied by coarse-grained molecular dynamics simulation. AAPS PharmSciTech. 2019;20(2):61.
36. Chovancova E, Pavelka A, Benes P, Strnad O, Brezovsky J, Kozlikova B, et al. CAVER 3.0: a tool for the analysis of transport pathways in dynamic protein structures. PLoS Comput. Biol. 2012;8(10):e1002708.
37. Izrailev SS S, Isralewitz B, Kosztin D, Lu H, Molnar F, Wriggers W, Schulten K. Steered molecular dynamics. Computational molecular dynamics: challenges, methods, ideas. Lect. Notes Comput. Sci. Eng. 1999(5):39−65.
38. Jarzynski C. Nonequilibrium equality for free energy differences. Phys. Rev. Lett. 1997;78(14):2690-3.
39. Bureau HR, Merz DR, Jr., Hershkovits E, Quirk S, Hernandez R. Constrained unfolding of a helical peptide: implicit versus explicit solvents. PLoS One. 2015;10(5):e0127034.
40. Homeyer N, Stoll F, Hillisch A, Gohlke H. Binding free energy calculations for lead optimization: assessment of their accuracy in an industrial drug design context. J. Chem. Theory Comput.. 2014;10(8):3331-44.
41. Izrailev S, Crofts AR, Berry EA, Schulten K. Steered molecular dynamics simulation of the Rieske subunit motion in the cytochrome bc(1) complex. Biophys. J. 1999;77(4):1753-68.
42. Grossfield A. WHAM: the weighted histogram analysis method. http://membrane.urmc.rochester.edu/content/wham/ , version 2.0.9.
43. Zhu F, Hummer G. Convergence and error estimation in free energy calculations using the weighted histogram analysis method. J. Comput. Chem. 2012;33(4):453-65.
44. Biedermannova L, Prokop Z, Gora A, Chovancova E, Kovacs M, Damborsky J, et al. A single mutation in a tunnel to the active site changes the mechanism and kinetics of product release in haloalkane dehalogenase LinB. J Biol Chem. 2012;287(34):29062-74.
45. Greene D, Qi R, Nguyen R, Qiu T, Luo R. Heterogeneous dielectric implicit membrane model for the calculation of MMPBSA binding free energies. J. Chem. Inf. Model. 2019;59(6):3041-56.
46. Miller BR, 3rd, McGee TD, Jr., Swails JM, Homeyer N, Gohlke H, Roitberg AE. MMPBSA.py: an efficient program for end-state free energy calculations. J. Chem. Theory Comput. 2012;8(9):3314-21.
47. Hac-Wydro K, Wydro P. The influence of fatty acids on model cholesterol/phospholipid membranes. Chem. Phys. Lipids. 2007;150(1):66-81.
48. Caliskan M, Poschmann G, Gudzuhn M, Waldera-Lupa D, Molitor R, Strunk CH, et al. *Pseudomonas aeruginosa* responds to altered membrane phospholipid composition by adjusting the production of two-component systems, proteases and iron uptake proteins. Biochim. Biophys. Acta Mol. Cell Biol. Lipids. 2023:159317.
49. Papackova Z, Cahova M. Fatty acid signaling: the new function of intracellular lipases. Int. J. Mol. Sci. 2015;16(2):3831-55.
50. Weiler AJ, Spitz O, Gudzuhn M, Schott-Verdugo SN, Kamel M, Thiele B, et al. A phospholipase B from *Pseudomonas aeruginosa* with activity towards endogenous phospholipids affects biofilm assembly. Biochim. Biophys. Acta Mol. Cell. Biol. Lipids. 2022;1867(4):159101.
51. Berman HM, Westbrook J, Feng Z, Gilliland G, Bhat TN, Weissig H, et al. The protein data bank. Nucleic Acids Res. 2000;28(1):235-42.
52. Sali A, Blundell TL. Comparative protein modelling by satisfaction of spatial restraints. J. Mol. Biol. 1993;234(3):779-815.
53. Murzyn K, Rog T, Pasenkiewicz-Gierula M. Phosphatidylethanolamine-phosphatidylglycerol bilayer as a model of the inner bacterial membrane. Biophys. J. 2005;88(2):1091-103.
54. Martinez L, Andrade R, Birgin EG, Martinez JM. PACKMOL: a package for building initial configurations for molecular dynamics simulations. J. Comput. Chem. 2009;30(13):2157-64.
55. Schott-Verdugo S, Gohlke H. PACKMOL-Memgen: A simple-to-use, generalized workflow for membrane-protein-lipid-bilayer system building. J. Chem. Inf. Model. 2019;59(6):2522-8.

56. Pashkovskaya AA, Vazdar M, Zimmermann L, Jovanovic O, Pohl P, Pohl EE. Mechanism of long-chain free fatty acid protonation at the membrane-water interface. Biophys. J. 2018;114(9):2142-51.
57. Salomon-Ferrer R, Gotz AW, Poole D, Le Grand S, Walker RC. Routine microsecond molecular dynamics simulations with AMBER on GPUs. 2. Explicit solvent particle mesh ewald. J. Chem. Theory Comput. 2013;9(9):3878-88.
58. Maier JA, Martinez C, Kasavajhala K, Wickstrom L, Hauser KE, Simmerling C. ff14SB: Improving the accuracy of protein side chain and backbone parameters from ff99SB. J. Chem. Theory Comput. 2015;11(8):3696-713.
59. Dickson CJ, Madej BD, Skjevik AA, Betz RM, Teigen K, Gould IR, et al. Lipid14: The amber lipid force field. J. Chem. Theory Comput. 2014;10(2):865-79.
60. Dickson CJ, Walker RC, Gould IR. Lipid21: complex lipid membrane simulations with AMBER. J. Chem. Theory Comput. 2022;18(3):1726-36.
61. Zhao CL, Zhao DX, Bei CC, Meng XN, Li S, Yang ZZ. Seven-site effective pair potential for simulating liquid water. J. Phys. Chem. B. 2019;123(21):4594-603.
62. Li P, Song LF, Merz KM, Jr. Systematic parameterization of monovalent ions employing the nonbonded model. J. Chem. Theory Comput. 2015;11(4):1645-57.
63. Sengupta A, Li Z, Song LF, Li P, Merz KM, Jr. Correction to "Parameterization of monovalent ions for the OPC3, OPC, TIP3P-FB, and TIP4P-FB water models". J. Chem. Inf. Model. 2021;61(7):3734-5.
64. Krautler V, Van Gunsteren WF, Hunenberger PH. A fast SHAKE: Algorithm to solve distance constraint equations for small molecules in molecular dynamics simulations. J. Comp. Chem. 2001;22(5):501-8.
65. Le Grand S, Gotz AW, Walker RC. SPFP: Speed without compromise-A mixed precision model for GPU accelerated molecular dynamics simulations. Comput. Phys. Commun. 2013;184(2):374-80.
66. Quigley D, Probert MI. Langevin dynamics in constant pressure extended systems. J. Chem. Phys. 2004;120(24):11432-41.
67. Berendsen HJC, Postma JPM, Gunsteren WFv, DiNola A, Haak JR. Molecular dynamics with coupling to an external bath. J. Chem. Phys. 1984;81(8):3684-90.
68. Lin YQ, Pan DY, Li JM, Zhang LX, Shao XM. Application of Berendsen barostat in dissipative particle dynamics for nonequilibrium dynamic simulation. J. Chem. Phys. 2017;146(12).
69. Marrink SJ, Berger O, Tieleman P, Jahnig F. Adhesion forces of lipids in a phospholipid membrane studied by molecular dynamics simulations. Biophys. J. 1998;74(2 Pt 1):931-43.
70. Schymkowitz J, Borg J, Stricher F, Nys R, Rousseau F, Serrano L. The FoldX web server: an online force field. Nucleic Acids Res. 2005;33(Web Server issue):W382-8.
71. Guerois R, Nielsen JE, Serrano L. Predicting changes in the stability of proteins and protein complexes: a study of more than 1000 mutations. J. Mol. Biol. 2002;320(2):369-87.
72. Tokuriki N, Stricher F, Schymkowitz J, Serrano L, Tawfik DS. The stability effects of protein mutations appear to be universally distributed. J. Mol. Biol. 2007;369(5):1318-32.
73. Subrini O, Sotomayor-Perez AC, Hessel A, Spiaczka-Karst J, Selwa E, Sapay N, et al. Characterization of a membrane-active peptide from the Bordetella pertussis CyaA toxin. J. Biol. Chem. 2013;288(45):32585-98.
74. Kovacic F, Bleffert F, Caliskan M, Wilhelm S, Granzin J, Batra-Safferling R, et al. A membrane-bound esterase PA2949 from *Pseudomonas aeruginosa* is expressed and purified from Escherichia coli. FEBS Open Bio. 2016;6(5):484-93.
75. Bertani G. Studies on lysogenesis. I. The mode of phage liberation by lysogenic Escherichia coli. J. Bacteriol. 1951;62(3):293-300.
76. Laemmli UK. Cleavage of structural proteins during the assembly of the head of bacteriophage T4. Nature. 1970;227(5259):680-5.
77. Ritchie TK, Grinkova YV, Bayburt TH, Denisov IG, Zolnerciks JK, Atkins WM, et al. Chapter 11 - Reconstitution of membrane proteins in phospholipid bilayer nanodiscs. Methods Enzymol. 2009;464:211-31.
78. Jaeger KE, Kovacic F. Determination of lipolytic enzyme activities. Methods Mol. Biol. 2014;1149:111-34.
79. Jayachandra K, Gowda MDM, Rudresha GV, Manjuprasanna VN, Urs AP, Nandana MB, et al. Inhibition of sPLA(2) enzyme activity by cell-permeable antioxidant EUK-8 and downregulation of p38, Akt, and p65 signals induced by sPLA(2) in inflammatory mouse paw edema model. J. Cell. Biochem. 2023;124(2):294-307.
80. Mahmood T, Yang PC. Western blot: technique, theory, and trouble shooting. N. Am. J. Med. Sci. 2012;4(9):429-34.
81. Urbani A, Warne T. A colorimetric determination for glycosidic and bile salt-based detergents: applications in membrane protein research. Anal. Biochem. 2005;336(1):117-24.